

Review

Analytical transmission electron microscopy for emerging advanced materials

Yue Lin,^{1,*} Min Zhou,² Xiaolin Tai,¹ Hangfei Li,² Xiao Han,¹ and Jiaguo Yu³

SUMMARY

With remarkable achievements in spatial resolution and its derived analytical techniques, transmission electron microscopy (TEM) has been capable of probing enriched information of materials at the atomic scale. Nevertheless, there seems to be a gap that hinders the further application of TEM-related techniques in the field of emerging advanced materials. This review presents the basic principles and functionalities of analytical TEM techniques in characterizing emerging materials. We focus on the advanced TEM techniques that, not only for observing the atoms or lattice, but also for providing deep insights from the TEM data. We categorize the recently prevalent analytical TEM techniques into advanced scanning TEM (STEM) resolving techniques, STEM-related data-processing techniques, electron energy loss spectroscopy (EELS) techniques, and *in situ* TEM techniques. This review is expected to promote the utilization of analytical TEM techniques in materials research and therefore to gain insights into the structure-performance relationships of emerging advanced materials.

INTRODUCTION

The ever-growing demands of sustainable energy supply and environment protection have raised global concerns in recent years. To overcome these challenges, numerous attempts have been made on the devices for energy storage/conversion and environment protection, such as lithium, potassium, and sodium-ion batteries,^{1–3} supercapacitors,^{4,5} solar cells,^{6,7} fuel cells, and metal-air batteries,^{8–10} where emerging advanced materials play significant roles in corresponding performances.

The performance of materials is strongly determined by their composition and structure at the atomic level. For instance, the catalytic activity of the catalysts depends on the coordination species, number, and configuration of the active atoms.^{11,12} Besides, the impacts of the crystalline phase, defects, and edge sites are also revealed in electrode materials of batteries and supercapacitors.^{13–15} Therefore, a detailed characterization of materials at nano- and atomic scale is desired to understand the structure-performance relationship, which is of importance for device improvements.

Analytical TEM, with the ability to visualize atomic-scale structures and chemical environments, has been regarded as an effective tool in material research since its invention in the 1930s. For most of its history, broad-beam techniques have been employed by TEM instruments, which has provided phase-contrast images of specimens. Since the 1990s, benefiting from the implementation of the aberration corrector, a significant improvement in the imaging resolution of TEM has been achieved. The remarkable resolving ability realized unprecedented observation of

¹Hefei National Laboratory for Physical Sciences at the Microscale, University of Science and Technology of China, Hefei 230026, China

²College of Physical Science and Technology, Yangzhou University, Yangzhou 225002, China

³State Key Laboratory of Advanced Technology for Materials Synthesis and Processing, Wuhan University of Technology, Wuhan 430070, China

*Correspondence: linyue@ustc.edu.cn

<https://doi.org/10.1016/j.matt.2021.05.005>



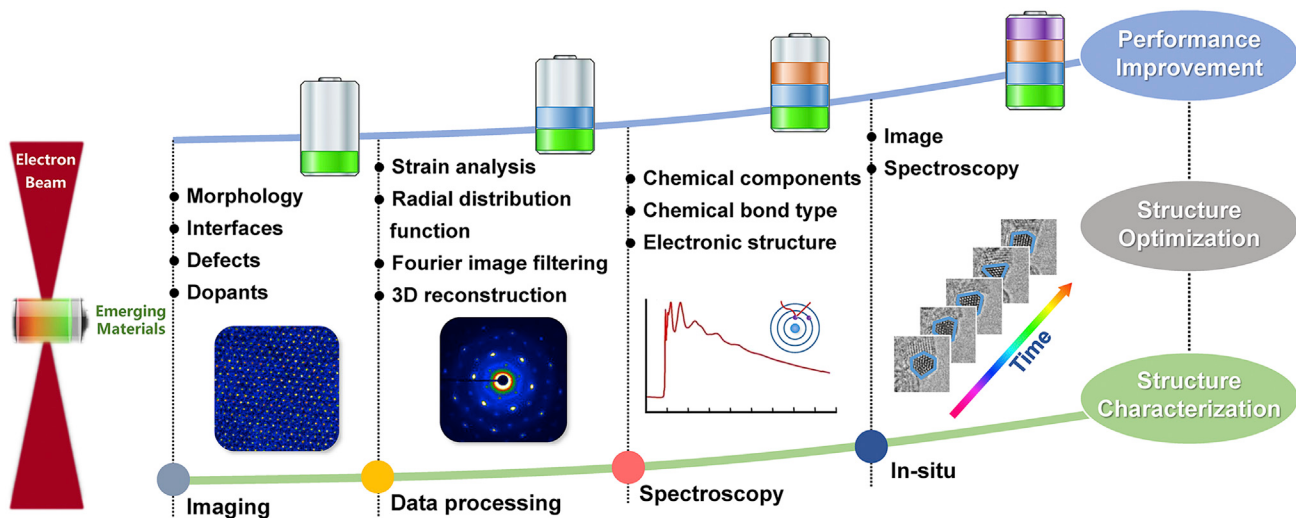


Figure 1. Schematic illustration of the analytical TEM techniques for emerging advanced materials

atomic structures. Most recently, Muller's group from Cornell University pushed the world record to 39 pm by using an electron microscope pixel array detector and ptychography technique.¹⁶ Furthermore, combined with spectroscopy techniques, such as EELS, the electronic structure of a specific atom can also be probed. Meanwhile, the development of *in situ* microscopy techniques allows for disclosing of material growth and transformation processes during chemical reactions.

Up to now, advanced TEM techniques are playing essential roles in studying the origins of functionalities of emerging advanced materials at the atomic level. Yet, the versatility of advanced TEM techniques, including the derived analytical approaches, has not been comprehensively utilized in practical studies. This is probably because of the gap between researchers from the materials field and the electron microscopy field. Here, based on the experiences of TEM and materials research in our group, we summarize the advanced analytical TEM studies developed for emerging materials characterization. Considering that comprehensive reviews of TEM techniques have been published previously,^{17–21} this review focuses on the advanced techniques not only to observe atoms but also to provide insights from TEM data. We categorize the emerging TEM techniques in terms of advanced STEM resolving techniques, STEM-related data-processing techniques, EELS techniques, and *in situ* TEM techniques (Figure 1). This review elaborates the brief principles and notable applications of the emerging TEM techniques, and aims to help the reader to conduct in-depth analysis of TEM data in materials research.

STEM TECHNIQUES

Conventionally, high-resolution (HR) TEM is dominated by the broad-beam technique that uses a parallel incident beam and collects coherent signals (Figure 2A). With a short signal collection time and favorable image resolution, HRTEM has been widely adopted in microstructure characterization. However, due to the important roles of specimen thickness and objective focus in contrast transfer function, the HRTEM image exhibits a strong thickness- and defocus-dependent nature. This makes the interpretation of the image difficult without careful consideration and simulations. Moreover, the resolving ability is limited by geometrical distortions of the wave-front caused by inevitable spherical and chromatic aberrations in the

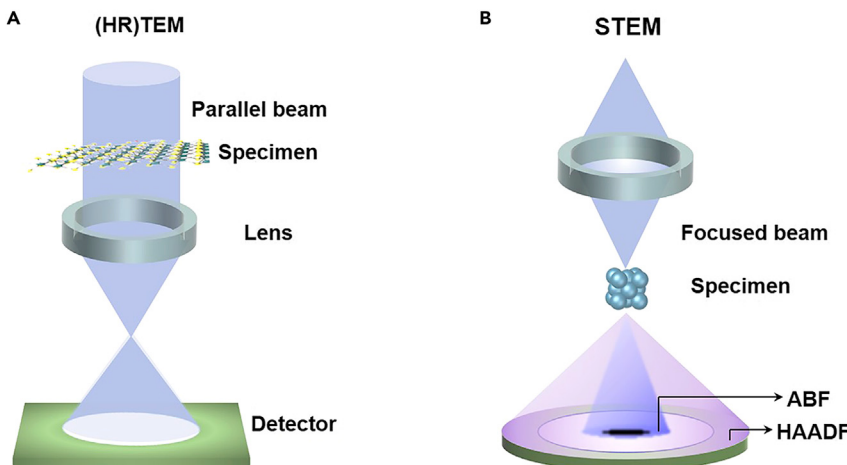


Figure 2. Typical imaging modes of (A) (HR)TEM and (B) STEM

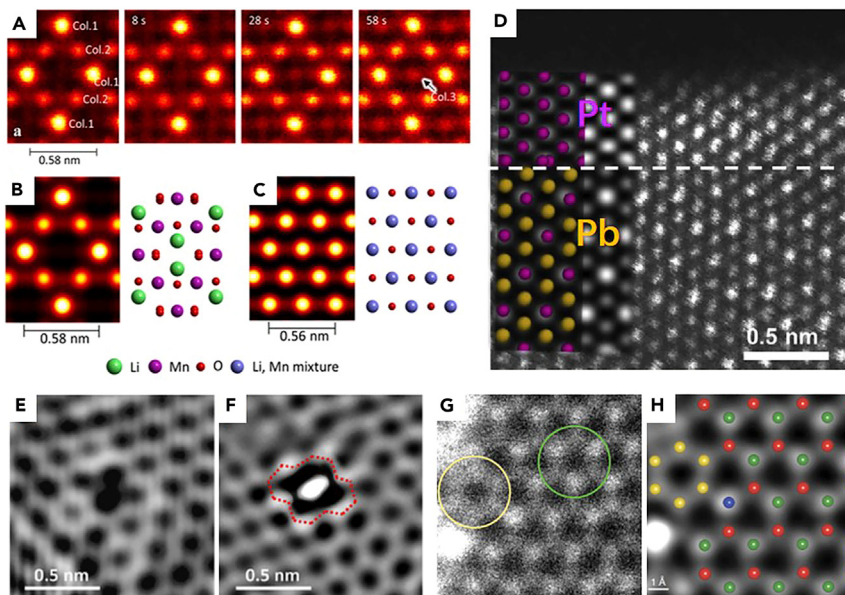
(A and B) Typical imaging modes of (A) HRTEM and (B) STEM.

instrument; the image contrast is easily affected by the amorphous layer on the specimen surface. Thus, it is difficult to extract a real atomic structure from the HRTEM image.

Despite the fundamental contributions in material characterization made by HRTEM, it is surpassed by STEM, especially implanted with an aberration corrector. STEM employs a convergent incident beam to scan the specimen point by point and collects the scattered electrons by detectors located at several geometric positions (Figure 2B). Although the process is time-consuming in image acquisition, STEM shows a significantly improved resolution and easier interpretation of obtained images compared with the conventional HRTEM. Moreover, images containing different information can be obtained by the detectors implanted in STEM with varied receiving angles, including high-angle annular dark-field (HAADF-STEM) imaging, middle-angle annular dark-field (MAADF-STEM) imaging, low-angle annular dark-field (LAADF-STEM) imaging, and bright-field (BF-STEM) and annular bright-field (ABF-STEM) imaging. The HAADF-STEM technique collects scattered electrons at high angles, usually 50 and 200 mrad for inner and outer angles, respectively. MAADF-STEM or LAADF-STEM images are obtained while the collecting inner angles are a little larger than the probe convergence. Among them, HAADF-STEM and ABF-STEM techniques have been widely performed in materials characterization due to the simple interpretation of the obtained images.

Z contrast imaging

Emerging advanced materials of different phase, interface, and defects, and dopant engineering into useful devices, are crucial for future energy storage/conversion and environmental protection. Conventional HRTEM can be used to characterize the phase, interface, and defects. However, the contrast reversal of HRTEM images brings some uncertainty, especially in the study of dopant engineering. In these cases, the STEM technique plays a more important role. The typical imaging mode for STEM is dark-field imaging, which receives scattering electrons from higher angles and realizes incoherent imaging, as shown in Figure 2B. As a result, the phase contrast almost disappears in dark-field imaging, and the image contrast will not reverse with the change of specimen thickness or defocus. The intensity of HAADF-STEM, I_{HAADF} , is approximately proportional to the square of atomic

**Figure 3. HAADF-STEM techniques for microstructure studies**

(A) HAADF-STEM images of the Li-Mn oxide, revealing the phase transition from spinel to rocksalt. (B and C) Simulated HAADF-STEM images of the two structured Li-Mn oxides. Reproduced with permission from Gao et al.²³ Copyright 2017, American Chemical Society.

(D) Interface HAADF-STEM image of the PtPb/Pt core/shell nanoplates. Reproduced with permission from Bu et al.²⁴ Copyright 2010, Springer Nature.

(E and F) The defective areas with vacancy (E) and atomic Ni trapped (F) on graphene. Reproduced with permission from Jiang and Wang.²⁵ Copyright 2018, Cell Press.

(G and H) (G) Recorded and (H) corrected for distortion, smoothed, and deconvolved HAADF-STEM image of oxygen, carbon-doped monolayer boron nitride. Reproduced with permission from Krivanek et al.²⁶ Copyright 2010, Springer Nature.

number Z : $I_{\text{HAADF}} \propto Z^2$. Therefore, the brightness of the spots in the image reflects the atomic number in real atomic columns so that the chemical composition information at atomic resolution can be obtained. Also, the intensity of HAADF-STEM is roughly proportional to the number of atoms in a column in a constant-composition specimen.²²

Having these advantages, HAADF-STEM is a powerful technique for phase identification, heterointerface characterization, and defect and dopant studies. For example, Gao et al. investigated the phase transition of $\text{LiMn}_2\text{O}_{4-\delta}$ from spinel to rocksalt structure by HAADF-STEM (Figure 3A).²³ The Li atom is tetrahedrally coordinated in the spinel structure, while in the rocksalt structure both Li and Mn are revealed in the octahedral sites (Figures 3B and 3C). This result provides direct evidence for understanding the degradation mechanism of Li-ion battery electrodes.

The heterointerface plays a crucial role in charge/energy transfer, lattice strain, dislocation, and space-charge effects. Bu et al. prepared PtPb/Pt core/shell nanoplates for the catalyst of oxygen reduction reaction (ORR).²⁴ The HAADF-STEM imaging technique revealed large biaxial tensile strain in the interfaces of the nanoplates (Figure 3D), from which the PtPb(hexagonal)/Pt(cubic) core/shell structure was confirmed. It also showed that the interfacial plane between PtPb and the edge-Pt layer differ from that between PtPb and the top (bottom) Pt layer. This unique structure brings compressive and tensile strain along different Pt planes, therefore boosting its ORR activity.

In recent years, the atomically dispersed catalyst has been an important research topic in the field of catalysis. HAADF-STEM imaging is a powerful tool to characterize single-atom catalysts.^{27–29} To reveal the configurations of single metallic atoms on graphene defects, Jiang and Wang imaged the defect (vacancy without and with the Ni single atom trapped) using a low-voltage HAADF-STEM technique (Figures 3E and 3F), providing direct evidence for understanding the enhanced electrocatalytic performance of hydrogen and oxygen evolution.²⁵

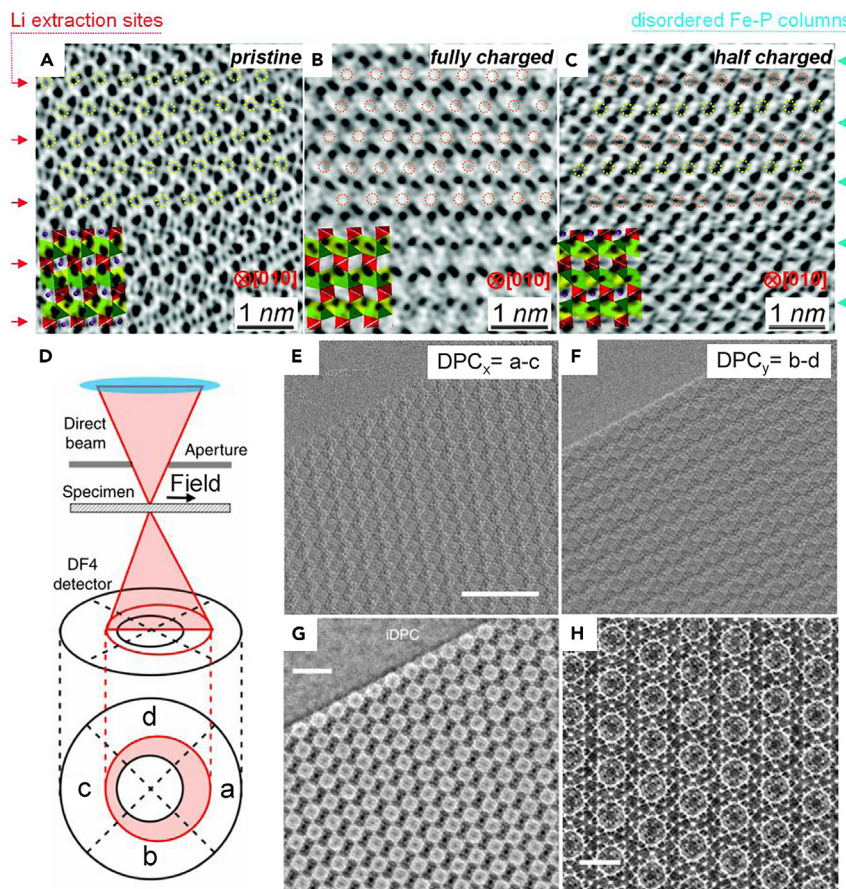
In principle, atoms with close atomic numbers, such as B, C, N, and O (Figures 3G and 3H),²⁶ and lighter elements distributed on heavier elements, such as Co atoms on monolayer MoS₂,³⁰ can be detected by HAADF-STEM contrast. Compared with conventional HRTEM, HAADF-STEM has advantages with higher spatial resolution, less dependence on the electron beam defocus, and thickness. And there is no proximity effects at interfaces or surfaces. However, light elements are challenging to image with HAADF-STEM, especially in the presence of heavier elements. Besides, HAADF-STEM needs a relatively long time for image acquisition and may exhibit image distortion caused by the drift of the specimen, making it unsuitable for fast *in situ* experiments. What's more, the intensity of the converged electron beam is sometimes too strong, leading to severe carbon contamination and damage of the specimen. Therefore, electron beam-sensitive materials are more suitable to be imaged at low-dose HRTEM or integrated differential phase-contrast (IDPC) mode.

Imaging of light elements

Understanding the distribution and migration of light elements, such as lithium, hydrogen, and oxygen in lithium batteries or hydrogen storage materials is essential for revealing the energy storage mechanism of these energy materials. For the imaging of light element materials, ABF-STEM is more suitable than HAADF-STEM.^{31,32} Due to the coherence of the electron beams collected at a small angle, ABF-STEM presents phase-contrast images. The contrast of ABF-STEM images shows less dependence on atomic number: $I_{ABF} \propto Z^{1/3}$. Therefore, light and heavy elements can be detected simultaneously in an ABF-STEM image, which is hardly achieved in HAADF-STEM images.^{33,34}

This unique ability makes ABF-STEM an effective tool in the characterization of electrode materials,^{35–38} such as spinel-structured LiMn₂O₄, LiV₂O₄, and LiFePO₄.^{39,40} Figure 4A shows a typical ABF image of pristine LiFePO₄, in which lithium columns, marked by yellow circles, can be well resolved. After being fully charged, all lithium columns disappear, as shown in Figure 4B. Interestingly, only part of the lithium columns can be seen after half charging (Figure 4C). A clear structural evolution process of electrode materials has been uncovered by ABF, which is conducive to understanding of Li transfer behaviors at atomic resolution.⁴⁰

In ABF images, light and heavy atomic columns have better visibility and interpretable robustness as the thickness changes. For thicker specimens, there is no reliable proportional relationship between the ABF intensity and the number of light atoms along the column. Thus, in a general way, atom counting cannot be achieved by ABF. And the visibility of light atom columns in ABF imaging is determined by the structure and direction of the material. Moreover, due to the poor signal-to-noise ratio and contrast reverse with defocus, it usually takes more time to acquire good ABF images than with HAADF. If the specimen is sensitive to the electron beam, it will be damaged before the ABF image is taken. To improve the signal-to-noise ratio, an enhanced annular bright-field (eABF-STEM) technique was developed by

**Figure 4. ABF and iDPC-STEM images**(A) ABF image of pristine state LiFePO₄.(B) ABF image of fully charged state LiFePO₄.(C) ABF image of half-charged state LiFePO₄, insets are the atomic structures. Lithium and delithiated columns are marked by yellow and orange circles, respectively. Reproduced with permission from Gu et al.⁴⁰ Copyright 2011, American Chemical Society.

(D) The schematic diagram of iDPC-STEM.

(E and F) The x and y components of the DPC image calculated as DPC_x = a-c (E) and DPC_y = b-d (F), respectively. Scale bar, 20 nm.

(G and H) The magnified iDPC-STEM image MOF MIL-101 material (G) with the highest resolution

(H). Reproduced with permission from Shen et al.⁴¹ Scale bars, 10 nm (G) and 5 nm (H). Copyright 2020, Springer Nature.

subtracting BF-STEM contrast from the ABF-STEM signal, facilitating the observation of light element materials.⁴² The iDPC technique is also good at imaging of light elements, as will be discussed below.

Electron beam-sensitive materials imaging

Electron beam-sensitive materials, such as metal-organic frameworks (MOF) and covalent-organic frameworks (COF), have broad applications in the fields of gas adsorption and storage, photoelectric conversion, heterogeneous catalysis, and energy storage and conversion. Revealing that its atomic structure is of great significance for understanding the relationship between its structure and performance, and for guiding the preparation of new emerging materials with excellent performance. Under normal circumstances, the electron beam will cause serious damage to its structure, and it is difficult to obtain real information of the structure, which

poses a severe challenge to TEM. Although ABF-STEM has been commonly used in imaging light elements, it is restricted by poor signal-to-noise ratio, contrast reverse with defocus, and thickness variations.⁴³ Another recently developed approach to probe the light elements in materials is iDPC, which uses differential phase-contrast (DPC) imaging with the four-quadrant detector in STEM. It physically analyzes the electrons collected in the bright-field area, and calculates the x and y components of the DPC image to obtain the final image after two-dimensional (2D) integration. The iDPC-STEM technique provides greatly improved sensitivity to light elements. Therefore, an ultra-low electron dose of $\sim 40 \text{ e}\AA^{-2}$ is sufficient to conduct the imaging, much lower than that needed in conventional HRTEM with atomic resolution ($>10^3 \text{ e}\AA^{-2}$).⁴⁴⁻⁴⁶ Besides, since the signal-to-noise-ratio (SNR) of iDPC-STEM images is higher than that of ABF-STEM images, the iDPC-STEM technology enables atomic-resolution imaging of beam-sensitive materials, such as MOF and COF, which usually suffer damages under high-energy electron irradiation.

MOF and polymeric materials have been widely applied in catalysis, gas storage, and adsorption separation. The iDPC-STEM technique is effective for studying the surface structure, defects, and interfaces of molecular sieve materials.⁴⁶ Shen et al. imaged the beam-sensitive MOF MIL-101 material using iDPC-STEM.⁴¹ Figure 4D displays the positions of the four detectors marked a-d, respectively. The x and y components of the DPC image were calculated as $DPC_x = a-c$ and $DPC_y = b-d$ (Figures 4E and 4F). After a 2D integration, the structure diagram MOF MIL-101 is obtained. As revealed in Figures 4G and 4H, more details can be extracted from the magnified iDPC-STEM image of the MIL-101 lattice. In particular, the corner-sharing super tetrahedrons consisting of the trimeric Cr nodes and 1,4-benzene dicarboxylate linkers were revealed. Likewise, Liu et al. used iDPC-STEM to study molybdenum on different zeolites and observed individual molybdenum clusters independently in the micropores, revealing that the diffusion of Mo atoms in the zeolites is affected by the backbone Al.⁴⁷

Cs-corrected low-dose HRTEM images have also been used to reveal the atomic structure of electron beam-sensitive materials. However, raw HRTEM images cannot be directly interpreted without the consideration of the contrast transfer function of the objective lens.^{48,49} Considering the excellent signal-to-noise ratio and less dependence on defocus and thickness, iDPC-STEM has advantages over low-dose HRTEM in imaging electron beam-sensitive materials. However, with regard to some very sensitive materials, the electron beam illumination of iDPC would still be too strong since it uses a converged electron beam.

Unlike BF, ABF, and HAADF, the iDPC-STEM imaging utilizes almost all electrons interacting with the specimen. Thus, compared with BF, ABF, and HAADF imaging with the same probe conditions, iDPC-STEM presents the better contrast and SNR for the specimens containing both heavy and light elements, which in the end provides the choice to image vulnerable samples under low-dose conditions.⁴⁶ iDPC has easily interpretable image contrast, as it approximately describes the local electrostatic potential distribution in the projection of thin specimen. iDPC-STEM also has its limitations and disadvantages. For instance, it suffers from significant contrast variation due to the thickness of the sample and the carbon contamination induced by the electron beam. Thus, iDPC-STEM requires the sample to be extremely thin, clean, and tilted right on the zone axis. Otherwise, the interpretation of the image is not so straightforward and confused information may be given. Also, it remains difficult to do iDPC-STEM image simulation for thicker specimens.

Another strategy to investigate electron beam-sensitive materials is cryoelectron microscopy (cryo-EM) that observes specimens frozen at low temperature. The cryo-EM technique was prominently applied in biological research to detect proteins. In 2017, Cui and co-workers first used cryo-EM to observe the changes of sensitive battery materials (Li metal dendrites) and discovered new atomic structures at the solid-electrolyte interphase (SEI).^{50,51} Since then, cryo-EM has shown great influence on battery research.^{52,53} Up to now, the application of cryo-EM has been gradually explored in other fields as well, such as perovskite solar cells, MOFs, electrocatalysts, and soft polymers.^{54–57}

STEM-RELATED DATA-PROCESSING TECHNIQUES

Accompanied with the progress in data-processing techniques, more analysis can be conducted using TEM to address in-depth understanding of atomic structures. In this section, we will introduce a useful data-processing techniques in TEM analysis that offers prominent physical and chemical insights for emerging advanced materials, including strain analysis, radial distribution function (RDF) and Fourier image filtering.

Strain analysis

For some energy materials, strains hold the promise of tuning the activity of catalysts, balancing the capacity and power density of batteries, and regulating the charge carrier behaviors in solar cells. Therefore, revealing the strain information of the materials, especially the strain distribution in the local region, is indispensable for understanding the performance enhancement caused by strain. Generally, strain measurements are performed by either coherent X-ray diffraction (XRD) or TEM. The TEM-based strain analysis methods, including peak-finding procedures and geometric phase analysis (GPA),^{58,59} provide higher spatial resolution than XRD and enables the visualizing of the strain field.

The peak-finding procedure is carried out by extrapolating the reference lattice to the deformed region, calculating the displacement vector for target lattice, then the local strain is calculated through derivation of the displacement.^{60–62} In parallel, the GPA method is an algorithm that uses Fourier and complex images to measure strains by analyzing images in reciprocal space. In this section, the applications of GPA in emerging materials are mainly introduced.

For the past few years, GPA has been used to measure lattice strains of emerging materials, especially for the lattice distortions caused by doping.^{63–66} By using GPA, Mao et al. obtained the ϵ_{yy} and ϵ_{xx} components of the strain tensor in Co-Ru nanoparticles. The doping of Co atoms into Ru catalysts makes the inner part of the nanoparticle more compressive than the outer part, thus compressing the Ru lattice and effectively controlling the selectivity of the catalysts in the hydrogenation reaction.⁶³

Defects, such as vacancies, dislocations, and grain boundaries, can be reflected by GPA techniques. Byeon et al. studied the Co dissolution behavior of LiCoO₂ in aqueous solution; the formation of cation vacancies after immersion in O₂ flow was directly observed by GPA, emphasizing the significance of the atomic structure in local stability of the cathode material.⁶⁷ The effect of intragranular cracks in the layer-structured cathode (LiNi_{1/3}Mn_{1/3}Co_{1/3}O₂) was also analyzed.⁶⁸ The strain distribution caused by the dislocation was presented by GPA analysis in the HAADF-STEM image (Figure 5A). In the strain map (ϵ_{yy}), the left and right side are under compressive

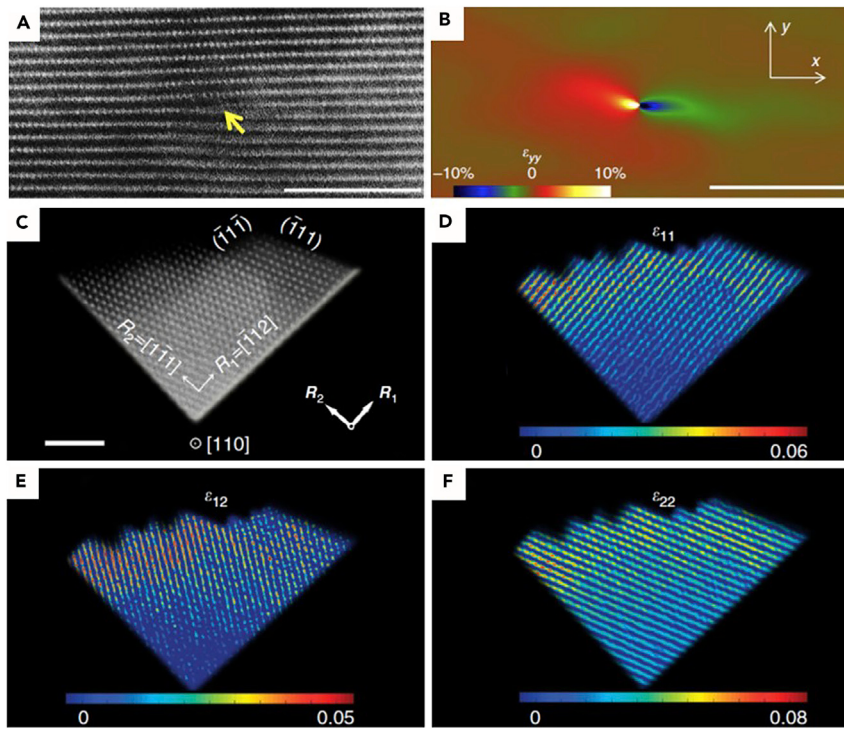


Figure 5. Strain analysis performed using the GPA technique

(A) HAADF image of $\text{LiNi}_{1/3}\text{Mn}_{1/3}\text{Co}_{1/3}\text{O}_2$ cathode that shows an end-on edge dislocation. Scale bar, 5 nm.

(B) The corresponding strain map by GPA. Reproduced with permission from Yan et al.⁶⁸ Scale bar, 5 nm. Copyright 2017, Springer Nature.

(C) HAADF-STEM image of CoO nanorods shows adjacent sawtooth-like edges enclosed with $\{111\}$ facets, in which the lattice vectors R_1 and R_2 are used as references for strain analysis. Scale bar, 2 nm.

(D–F) Contour plots of the strain component ϵ_{11} (D), ϵ_{12} (E), and ϵ_{22} (F) relative to the reference values. Reproduced with permission from Ling et al.⁷¹ Copyright 2017, Springer Nature.

and tensile strains, respectively (Figure 5B). Also, the strains caused by the grain boundaries were also revealed in the materials of the lithium anode and the HER catalyst, providing solid evidence for the improving effect of the heterostructures.^{69,70}

GPA techniques are also applied in determining the phase changing and morphological evolution of materials by visualizing the strain distributions, which are of great importance to tailor their electronic properties.^{71–73} Ling et al. prepared CoO nanorods (CoO NRs) using a cation exchange method. During this process, an apparent strain-induced morphological evolution of the sample surface was produced.⁷¹ With the assistance of HAADF-STEM and GPA (Figure 5C), it is found that the lattice strain components, ϵ_{11} and ϵ_{22} , are correlated with the expansion/contraction of the corresponding lattice vectors R_1 and R_2 (Figures 5D–5F). The values of ϵ_{11} , ϵ_{12} , and ϵ_{22} in the inner part of the CoO NR are approximately zero, and become positive on the outermost surface of the sawtooth-like structure (Figures 5D–5F). These results indicate that the tensile strain induced by the cation exchange method is distributed in the uppermost part of the CoO NRs, which facilitates the regulation of the electronic structure, generates O vacancies, promotes the dissociation of water, optimizes the adsorption of hydrogen, and thus improves its HER performance.

Both peak-finding and GPA procedures are sensitive to noise and high signal-to-noise images are required to extract strain information. Compared with the peak-finding procedures, a remarkable advantage of GPA is that the information is obtained from a local region in Fourier space, thus minimizing the optical aberrations in the instruments.⁷⁴ It is useful for strain measurement when defects or large displacements are in the presence of sample region. However, GPA does not make full use of the information of atomic-resolution images and requires that phase varies slowly. Thus, GPA is only suitable for certain images, such as dot-like HRTEM and STEM images. If using STEM images, one should be careful about the distortion and drift of the specimen caused during image acquisition. Besides, GPA is limited to process strain imaging analysis in a small field of view and cannot be used in analyzing an amorphous region and crystal discontinuities.

Atomic radial distribution

Characterization of the localized atomic structure in amorphous materials remains challenging due to the lack of long-range order and variation of coordination numbers over the atomic scale. RDF, which describes the density function of surrounding particles or atoms, is an important structural characteristic to the performance of the amorphous materials.⁷⁵ RDF can be experimentally measured from electron diffraction (ED), neutron diffraction (ND), or XRD, by converting the diffraction data into information about nearest-neighbor distances and coordination numbers. Nevertheless, neutron and XRD experiments yield average information of specimens so that plenty of signals are probably hidden in heterogeneous materials. In contrast, the combination of RDF and TEM techniques allows sampling an area of several nanometers, thus providing great potential for understanding nano-scale structural variations. In detail, the peaks of RDF in the image contain three types of information: the location of each peak represents the radius of each coordination shell layer, the integrated area of the peaks reflects the number of atoms in each coordination shell layer, and the width of the peaks is associated with the uncertainty of the atomic positions caused by the static disorder and thermal dynamic disorder effects.

Atomically disordered structure with abundant defects and coordination unsaturated sites usually endows amorphous structures with unique properties in the area of energy and environment applications.⁷⁶ Wu et al. suggested a general method for synthesizing amorphous noble metal nanosheets.⁷⁷ To characterize the local structural of the specimens, RDF values of amorphous and crystalline Ir nanosheets (Ir NSs) were obtained (Figures 6A and 6B); peaks R_{nea} and R_{sec} refer to the average distance of the nearest and second nearest-neighbor Ir atoms, respectively. The broadened and shifted peaks toward higher distances in the amorphous Ir NSs proved the poor periodicity of corresponding atomic structures. In addition, RDF was used to probe the kinetics of nanoparticle formation. Gao et al. studied the material transformation process from the K_2PtCl_4 precursor to Pt nanoparticles in solid state.⁷⁸ By integrating the RDF and spectroscopy data captured in real space, it was proposed that the K_2PtCl_4 precursor is first decomposed into K^+ and PtCl_4^{2-} due to weak ionic bonds (Figures 6C and 6D).

RDFs acquired from ED, ND, or XRD have corresponding advantages and limitations. The physical meaning of RDF is the number of atoms at the distance r from the central atom, which represents the spherical symmetric radial distribution state of surrounding atoms:

$$\text{RDF}(r) = 4\pi r^2 \rho(r), \quad (\text{Equation 1})$$

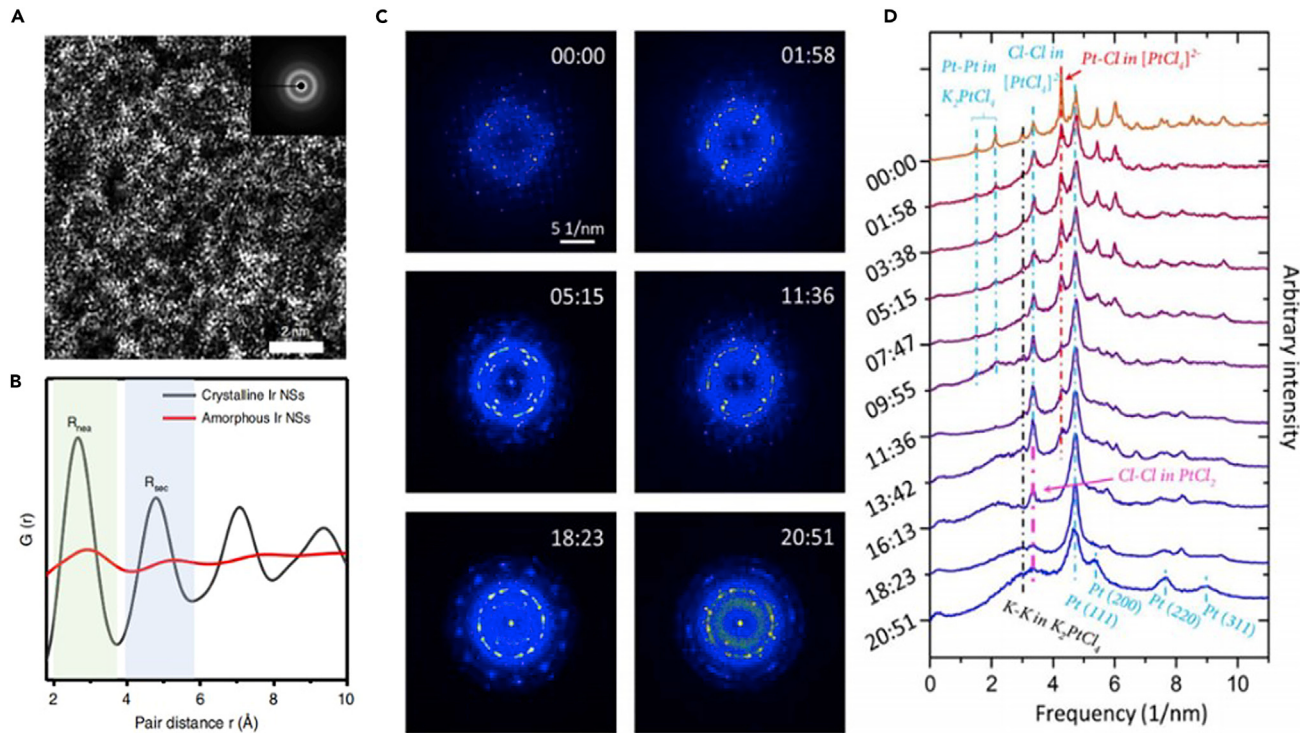


Figure 6. RDF technique in analysis of localized atomic structure of amorphous materials

(A) HAADF-STEM image of amorphous Ir NSs. The inset in (A) is the selected area electron diffraction pattern.

(B) RDF of amorphous and crystalline Ir NSs, respectively. Reproduced with permission from Wu et al.⁷⁷ Copyright 2019, Springer Nature.

(C) Time series diffractogram using FFT from sequential low-dose images during K₂PtCl₄ decomposition.

(D) RDF derived from the sequential diffractogram in (C). Reproduced with permission from Gao et al.⁷⁸ Copyright 2019, the American Association for the Advancement of Science.

where $\rho(r)$ is the atomic number density at distance r from the central atom.

In brief, after absorption correction, normalization treatment deducting the incoherent scattering, and Fourier transform, the RDF could be calculated according diffracted intensity as follows:

$$\text{RDF}(r) = 4\pi r^2 \rho_a + \frac{2r}{\pi} \int_0^\infty s[i(s) - 1] \sin sr ds, \quad (\text{Equation 2})$$

where $s = 4\pi \frac{\sin \theta}{\lambda}$ (θ is the angle of incidence, λ is the wave length) is the scattering vectors; ρ_a is the average atomic number density of sample; $i(s)$ is the structure factor, which could be deduced from diffracted intensity: $I(s) = Nf^2 i(s)$, $I(s)$ is the diffracted intensity, N is the number of atoms involved in diffraction, and f is the atomic scattering factor.⁷⁹

It is clear from the above calculation protocol that the differences between the RDF acquired from XRD, ED, and ND are mainly situated at the different light source. As shown in Equation 2, the integration is conducted in the whole space of s ; however, there is an upper limit of s accessible in the experimental test. The upper limit value, s_{\max} , is dependent on the angle of incidence θ and wave length λ . Larger θ and shorter λ raise the upper limit and thus provide more detailed structural information about atomic pair distribution. As the λ of ND is relatively longer, θ is small and the precision of θ detection is limited in ED. XRD, particularly the one based on

synchrotron radiation, shows the highest accuracy in structure analysis. However, the information acquired from XRD is the average value macroscopically. ND shows an advantage in detecting light atoms, magnetic atoms and isotopes, and analysis for detailed structures, but has much weaker intensity relative to synchrotron radiation X-rays (several orders of magnitude).⁸⁰ On the other hand, ED is suitable in probing tiny areas and has high spatial resolution. Moreover, the diffracted intensity not only includes information from structure of materials but also unrelated background parts, such as incoherent scattering, multiple scattering, and absorption, which also influence the result of RDF. Because X-ray and electron flow mainly adopt the electron in the atom as the scattering center, while neutrons interact with the nucleus, ND displays stronger penetrability and weaker absorption. In summary, RDFs calculated from the three diffraction technologies have their respective pros and cons, and need to be combined in practical application.

Fourier image filtering

During electron microscopy imaging, there may be cases that lead to low signal-to-noise ratios, amorphous signals on the background, and multiple samples superimposed, resulting in unclear or complex images. After the images have been taken, one can also try to improve the image quality and highlight the feature. Fourier filtering is a powerful method to highlight the feature, remove the noise, and enhance the quality of the image by conducting continuous fast Fourier transform (FFT) on either HRTEM or HAADF-STEM images. In a basic operation, an FFT process is used to convert original images with lattice or atomic fringes into FFT patterns in reciprocal space. To eliminate the disturbance caused by poor crystalline or imaging noise, a mask/filter is applied to subtract the undesired signal around the target spots in the Fourier space.⁸¹ Subsequently, an inverse Fourier transformation is processed to gain a filtered real-space image that contains sharpened and clarified information. Therefore, the Fourier filtering technique has been widely adopted in materials because of the enhanced ability to visualize crystal structures and defects.^{82–84}

The selection of region-of-interest tools for specific regions is very important for quantitative image interpretation, such as grain boundary interfaces, atomic defect regions, alignment regions with atomic alignment, etc. In addition, there are many filter algorithms, such as spot, bandpass, array, and wedge filter masks provided in the Gatan DigitalMicrograph (DM). One can also develop new filters as needed. Therefore, choosing a suitable filter is critical to correctly obtain or highlight image information. For instance, compared with the Wiener filter, the average background subtraction filter (ABSF) will average the contrast of the bright spots in the image. Therefore, if one wants to highlight the image with single-atom loading or doping, ABSF is not suitable.⁸¹

With regard to visualization of defects, Han et al. studied the disordered lattice structure with crystal defects and edge dislocations at the F-Co₂B interface by Fourier filtering techniques, which validates a new strategy to engineer the crystalline-amorphous interface for high-performance catalysts toward water oxidation.⁸⁵ Similarly, Jung et al. used a Fourier filtering method to study the defects in CdS/CdSe co-sensitized ZnO nanowires in solar cells. By observing the density and location of dislocations on the interfaces, they found that the dislocation density of the CdS layer in a ZnO/CdS/CdSe structure was considerably lower than that in a ZnO/CdS structure, illustrating the roles of defects in photovoltaic performance (Figures 7A–7D).⁸⁶

Intermetallic nanoparticles have achieved great success in catalysis by forming ordered phases, while recognizing that the phase transition process is a crucial step

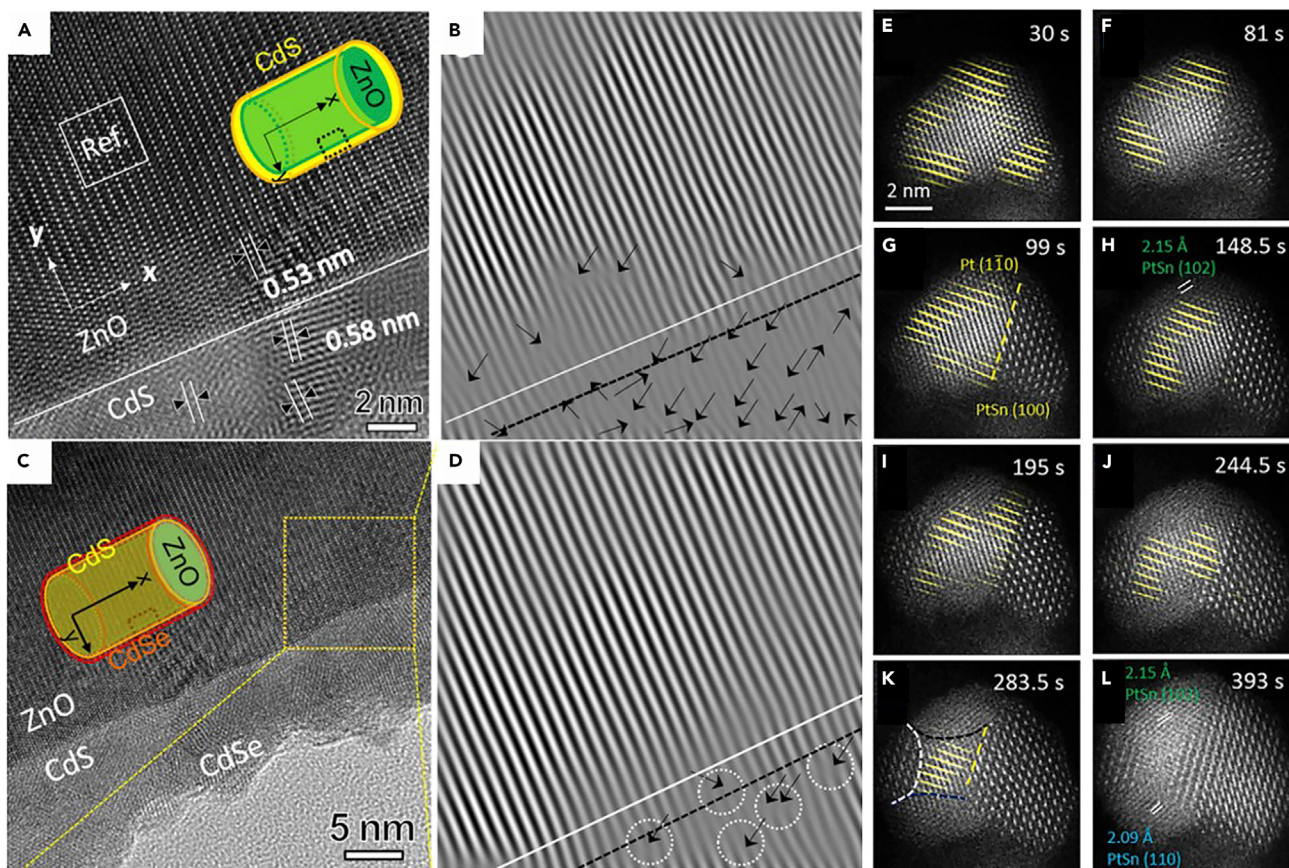


Figure 7. Fourier image filtering for lattice and atomic fringe analysis

(A) HRTEM and (B) Fourier filtered images of the CdS-ZnO interface. (C) HRTEM and (D) Fourier filtered image of the CdSe-CdS-ZnO interface. Reproduced with permission from Jung et al.⁸⁶ Copyright 2016, Elsevier.

(E–L) Sequential HAADF-STEM images of the growth of mSiO₂-encapsulated Pt/SnO₂, demonstrating the growth of Pt₃Sn and PtSn. The images were superimposed with Fourier filtered image (yellow), produced generated from the superlattice spots of Pt₃Sn. Reproduced with permission from Ma et al.⁸⁷ Copyright 2019, Elsevier.

to reveal the transition mechanism. By superimposing a Fourier filtering technique on HAADF-STEM images, Ma et al. revealed a gradual transformation of the Pt \rightarrow Pt₃Sn \rightarrow PtSn phase during the reaction between SnO₂ and Pt. The results support that the control of phase and catalytic activity can be achieved in the transformation process, providing valuable guidance for the designed synthesis of intermetallic catalysts⁸⁷ (Figures 7E–7L). Similar phase transformation processes in Cu_{2-x}Se and HfO₂ were also uncovered by the Fourier filtering method, which helps in the study of the stabilization of inaccessible sub-stable structures in bulk materials.^{88,89}

3D reconstruction

The phase and composition distribution of nanomaterials in 3D space determines their properties. Traditional TEM analysis usually obtains 2D projections of 3D objects, which in some cases is not enough to reflect the real structures. Recently, electron tomography (ET) has been developed to present the 3D structure of nanomaterials at the atomic scale. ET is a method that takes multiple 2D projections of samples with different rotation angles by rotating the holder, and combines them with reconstruction algorithms to obtain an accurate reconstruction of 3D objects.

By using ET, finer features of complex nanostructures can be distinguished than ever before. It can also be combined with advanced energy spectrum techniques, such as energy-dispersive X-ray spectroscopy (EDS) and EELS for 3D chemical composition and state analysis. Combining aberration-corrected electron microscopy and powerful 3D image reconstruction atom-tracking algorithms, Miao et al. developed a groundbreaking atom ET (AET),⁹⁰ which can accurately determine the 3D coordinates of individual atoms in materials. The highest resolution has reached 0.7 Å. Goris et al.⁹¹ obtained the coordinates of all atoms in a nanoparticle by assuming that the 3D atomic potential can be modeled by 3D Gaussian functions. Thus, the 3D strain analysis can be done.⁹¹ This technique cannot only measure the strain tensor at the atomic scale but also provide a direct tool for determining the atomic structure of amorphous materials. ET quantitative analysis further promotes this imaging technique to be applied to extensive fields, such as defect identification, pore structure analysis, long/short-range sorting, and atomic-level differentiation of precise components.⁹² The rapid 3D reconstruction combined with *in situ* technology can directly visualize the 3D structure changes of nanomaterials under environmental changes, and reveal the relationship between the 3D structure and properties of materials under actual conditions.⁹³

Despite the rapid development of ET technology in recent years, there are still limitations. First, in the process of data collection, the sample is recorded at a series of tilt angles, but the rotation of the sample holder is restricted, resulting in the missing wedge. This loss of information greatly damages the reconstruction resolution. Using specially designed sample rods and 360° ET technology, improvement of resolution is being explored.⁹⁴ Second, to maintain the reliability of the data, the ET process requires long-term exposure, and brings large amounts of electron irradiation on the sample, which may cause damage, especially for soft materials and organic hybrid materials. Using low-dose and low-temperature imaging of objects is a viable option.⁹⁵ Also, improving the data acquisition rate is an alternative route to realize the rapid analysis of complex materials. Also, currently, discontinuous photography methods cannot capture the full details of structural changes. Advanced reconstruction algorithms are desired to track the dynamic processes of materials under real conditions.

EELS TECHNIQUES

Spectroscopic techniques are used to conduct elemental analysis by employing detectors integrated within electron microscopes. Among them, EDS detects the X-rays generated by the interaction between the incident electron beam and the specimen, which has been already widely utilized. To improve the detection efficiency of X-rays, EDS manufacturers usually use two symmetrical or perpendicular large-area EDS detectors to collect X-rays. There are also manufacturers that integrate four symmetrical EDS detectors into the pole piece to collect X-rays. The solid angle of X-ray detection of a single commercial EDS has already reached 1.4 steradians (sr). With two detectors, solid angles of greater than 2.8 sr are achievable. The EDS energy resolution for TEM reaches 126 eV; however, this is still much lower than that of EELS. Combined with spherical aberration correction electron microscopy, the spatial resolution of EDS mapping can be as low as 140 pm. Identification of a single atom using EDS has been demonstrated.⁹⁶

Another spectroscopic technique in TEM is EELS. EELS detects the energy loss caused by the inelastic scattering between the incident electron beam and the sample. In general, EDS is a better method to detect heavy elements, while EELS is good

Table 1. Comparison between EDS and EELS in TEM

	EDS in TEM	EELS in TEM
Signal-to-background ratio	high	medium or low
Thickness requirements	both thin and thick	thin
Detection efficiency	low	high
Element range	better for heavy elements	better for light elements
Specimen at high temperature	dose not work	work
Energy resolution	low	high
Signal interference from TEM column and grid	yes	no
Information provided	only chemical	chemical and electronic
Ease of use	simple	complex
Ease of interpretation	simple	complex
Carbon contamination sensitive	no	yes

at probing light elements. Up to now, both EDS and EELS can realize atomic resolution in elemental mappings. A complete comparison is shown in [Table 1](#).

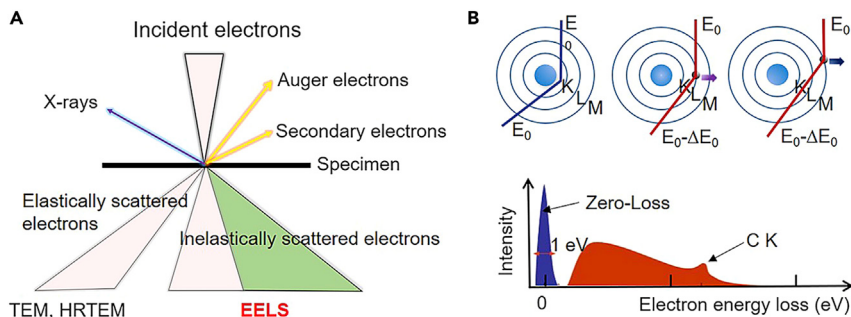
In addition to elemental distribution, EELS could also provide detailed electronic structures on the local atoms, which is extremely useful to the study of battery electrodes and catalysts. Compared with EELS, EDS has already been extensively utilized in materials research. Therefore, in this section, EELS will be discussed in detail.

EELS was first developed to detect carbon, silicon, oxygen, and other light elements.^{97–99} After a series of improvements, EELS has become a crucial technique to detect the chemical compositions and electronic structures of materials.

EELS measures the energy distribution of incident high-energy electrons after inelastic scattering with the specimen. In the case of incident electrons scattered with the specimen, the collected electrons consist of elastic and inelastic scattering electrons ([Figure 8A](#)). The spatial environment information of electrons in atoms can be obtained according to the energy loss spectra, further inferring the physical and chemical properties of specimens.

According to the energy loss range, EELS is typically separated into three regions: zero loss, low energy loss, and high energy loss regions ([Figure 8B](#)). The zero loss region ($E = 0$ eV) mainly includes transmitted electrons that experienced elastic scattering without energy loss. It is mainly used for instrument calibration¹⁰⁰ and energy-filtered imaging.¹⁰¹ The low energy loss spectrum ($\Delta E < 50$ eV) is associated with electrons experiencing phonon, inter/intraband transitions, and plasmon excitations. The low energy loss spectrum is typically used to measure the specimen thickness, electron gaps, electron density, and other relevant information. The high energy loss spectrum ($\Delta E > 50$ eV), also called the core-loss spectrum, is mainly caused by the inelastic scattering between the incident electrons and the electrons in the inner shell of the atoms. The energy loss during this process reveals information, such as the composition, bonding, and electronic configurations of the elements.

Compared with traditional spectroscopy techniques in TEM, such as EDS, EELS shows an ultra-high-energy resolution in the element analysis. The energy resolution of EELS has reached 4.2 meV without cost of spatial resolution, which is almost 5 orders of magnitude higher than that of EDS.⁹⁹ In addition, EELS is more useful to

**Figure 8. The schematic diagram of EELS**

(A) The interaction between incident high-energy electrons and specimens.

(B) EELS signal generation.

detect light elements. More importantly, emerging progress for EELS is being combined with high-resolved STEM enabling the analysis of such spectra over the atomic scale, making it a cutting-edge method for energy materials research.

Low-energy loss spectra

Plasma excitation spectrum

Plasma excitation refers to the inelastic scattering of incident electrons with the valence electrons of the sample, during which valence electrons experience a collective plasma resonance called plasmon.

Plasma excitation spectra recorded by EELS can be used to quickly estimate the thickness of the specimen.¹⁰² With the increasing thickness, the intensity in the plasma region of EELS increases, while the intensity of the zero-loss peak decreases. There are several methods for measuring the thickness of a sample in TEM. Among them, the method using the plasma excitation spectrum is the quicker one, although it is only a rough estimation. Based on this, Collins et al. revealed the thickness map of the lanthanum-doped ceria nanocatalyst (Figures 9A and 9B) by the EELS-STEM technique.¹⁰³

The surface-bound optical excitations in metallic nanoparticles have been widely involved in photocatalysis, nanometer integrated photonics, optical sensing, and solar cells. Collective oscillations of the valence electrons, also called plasmons, can be directly excited by fast electrons. By energy conservation, the energy losses of electron beam correspond to the excitation energies. EELS measures the energy loss of the electron beam, making it an excellent method to probe plasmon oscillations. The plasma excitation spectrum recorded by EELS can image localized optical excitations with high resolution to reveal the dielectric constant and charge density distribution of the materials over the region of interest.¹⁰⁵ Recently, the 3D images of localized surface plasmon resonances were obtained by measuring the plasma excitation spectrum of a nanoparticle at different orientations (Figures 9C and 9D).¹⁰⁴ Nelayah et al. applied EELS on the silver nanotriangles to achieve nanoscale resolution by detecting the plasmon as the resonance peaks in the near-infrared/visible/UV domain.¹⁰⁵ They plotted the EELS amplitude maps of different modes to connect the EELS signal with the local electromagnetic density of states in thin nearly planar systems, which can produce the electronic density of states-eigenmode (Figures 9E–9H). These results extended the knowledge in the optical responses of noble metal nanoparticles.

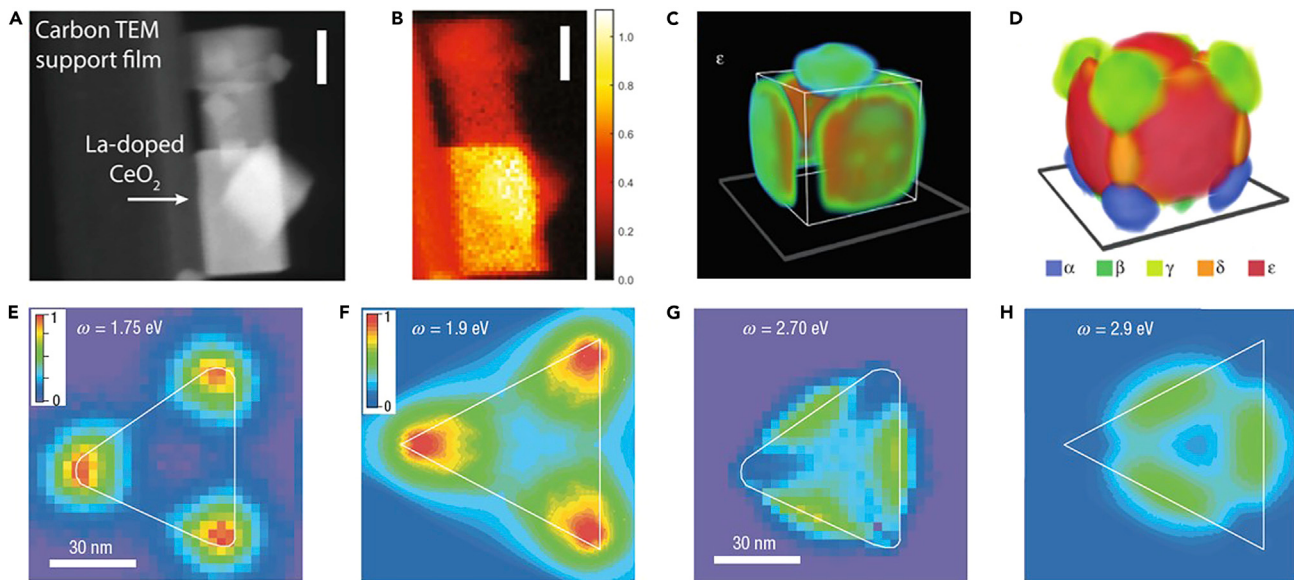


Figure 9. Plasma excitation in measuring local properties of nanomaterials

(A) ADF-STEM image of La-doped CeO_2 nanoparticle. Scale bar, 25 nm.

(B) Thickness map of an La-doped CeO_2 nanoparticle. Reproduced with permission from Collins et al.¹⁰³ Copyright 2017, Springer Nature. Scale bar, 25 nm.

(C and D) 3D visualization of the localized surface plasmon resonance components of a silver nanocube. Reproduced with permission from Nicoletti et al.¹⁰⁴ Copyright 2017, American Chemical Society.

(E) EELS amplitude maps on the silver nanotriangles of different modes centered at 1.75 eV.

(F) EELS amplitude maps on the silver nanotriangles of different modes centered at 1.9 eV.

(G) EELS amplitude maps on the silver nanotriangles of different modes centered at 2.70 eV.

(H) EELS amplitude maps on the silver nanotriangles of different modes centered at 2.9 eV. Reproduced with permission from Nelayah et al.¹⁰⁵ Copyright 2007, Springer Nature.

Band gap

Band gap measurement is a substantial application for EELS. When receiving energy higher than the band gap, the valence electrons experience a transition from the valence to the conduction band. Therefore, the energy loss of the incident electrons equals that of the band gap width, which can be detected by the instrument. By integrating the EELS data into STEM, the band gap information of a local area in the specimen can be obtained, which is a straightforward strategy to investigate the effects of microstructures on the materials band gap.

Virdi et al. investigated the band gap of layered perovskite nanosheets using STEM-EELS.¹⁰⁶ As shown in Figures 10A–10C, the monolayer perovskite nanosheet was confirmed by STEM. A band gap of 2.9 ± 0.2 eV was measured for the monolayer perovskite nanosheet, which is 0.2 eV lower than that of the bulk perovskite (3.1 ± 0.1 eV). This trend is inconsistent with that obtained by the UV-vis spectra. Combined with the high spatial resolution capability of STEM, Prytz et al. showed the 2D distribution of the band gap width of the $\text{Zn}_{1-x}\text{Cd}_x\text{O}/\text{ZnO}/\alpha\text{-Al}_2\text{O}_3$ multilayer structure, which was produced by directly analyzing the band gap energies in EELS. Since there is quantitative correlation between band gap energy and plasmon energy, the band gap mapping can also be reconstructed from the plasmon energy map (Figure 10D).¹⁰⁷ Based on EELS, the sub-band gap defect levels in other semiconductors were also measured, such as AgCuInGaSe_2 and BAIN thin films in the BAIGaN alloys system,^{108,109} highlighting the potential of STEM-EELS in semiconductor characterization.

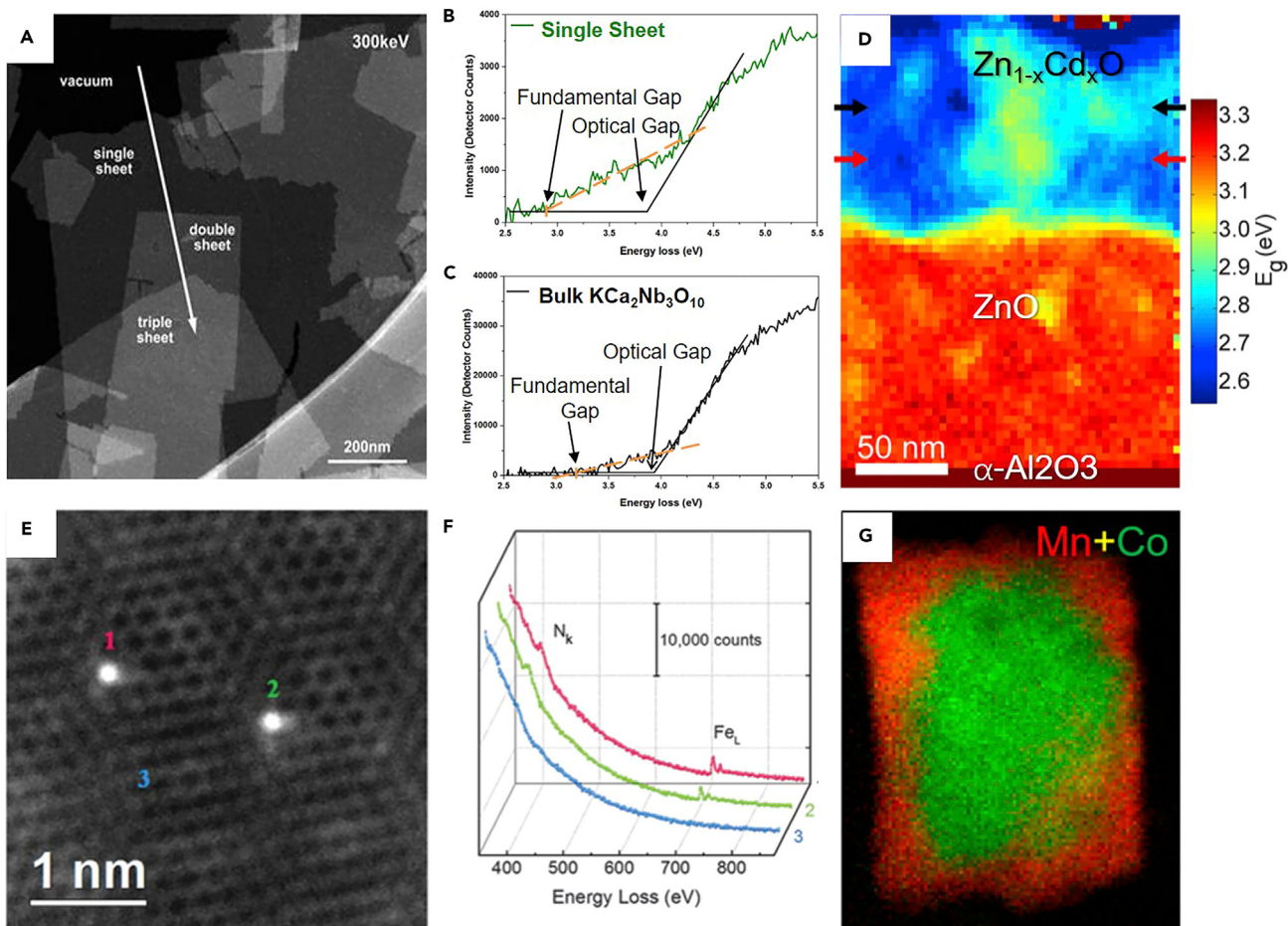


Figure 10. Local band-gap analysis and elemental analysis conducted by EELS

- (A) HAADF-STEM image of the perovskite nanosheets.
- (B) The EELS spectrum taken from the single perovskite nanosheets.
- (C) The EELS spectrum taken from the bulk perovskite. Reproduced with permission from Virdi et al.¹⁰⁶ Copyright 2016, American Chemical Society.
- (D) Band-gap mapping reconstructed from the plasmon energy map. Reproduced with permission from Zhan et al.¹⁰⁷ Copyright 2018, Springer Nature.
- (E) HAADF-STEM image of individual Fe atoms (labeled 1, 2, and 3) in a few-layer graphene sheet.
- (F) EELS of the N K-edge (N_K) and Fe L-edge (Fe_L) obtained from single atoms (1 and 2) and few-layer graphene (3). Reproduced with permission from Chung et al.¹¹⁰ Copyright 2017, the American Association for the Advancement of Science.
- (G) EELS mapping of Mo and Co elements, showing the Co-Mn core-shell structure of $\text{MnCo}_2\text{O}_4/\text{C}$. Reproduced with permission from Yang et al.¹¹¹ Copyright 2019, National Academy of Science.

Core-loss spectra

Elemental analysis

As discussed above, the elements in the specimen determine the EELS peak position and intensity. This feature has been utilized to probe the elemental information. The K-absorption edge is usually used to analyze the elements with atomic numbers less than 13, while it is used for L- or M-edges for heavier elements.

Compared with EDS, EELS is more effective in probing light elements, such as C, N, and O. Cosandey et al. used EELS to detect O, Mn, and Ni in $\text{LiMn}_{1.5}\text{Ni}_{0.5}\text{O}_4$ electrode material.¹¹² Moreover, the position and coordination of a single atom can be directly probed by STEM-EELS. Chung et al. developed Fe-N-C polyporous catalysts, in which the Fe atomically dispersed in a graphene substrate.¹¹⁰ As shown in the HAADF-STEM image (Figure 10E), the bright dots (marked as 1 and 2) on

graphene indicate the existence of monodispersed heavier atoms, which were further identified to be Fe atoms by the EELS spectra (Figure 10F). Nitrogen signals were captured around the Fe atoms, whereas it had not been detected in the Fe-free region (3), confirming the Fe-N coordination in the catalyst.

Combining STEM and EELS, the 2D distribution of elements, also called EELS mapping, can be produced. Yang and co-workers studied several spinel catalysts for fuel cells, including MnCo₂O₄/C, CoMn₂O₄/C, and CoFe₂O₄/C. They found that the MnCo₂O₄/C with unique Co-Mn core-shell structure, revealed by EELS mapping, exhibits most excellent performance (Figure 10G).¹¹¹ With the help of the Cs-corrector, the spatial resolution can reach atomic scale. Similarly, Wang and co-workers adopted EELS mapping to show the atomic-scale distribution of O, Mn, Co, and Ni in LiNi_{1/3}Mn_{1/3}Co_{1/3}O₂ (NMC333) layered cathode in a lithium-ion battery. The well-preserved layered and disordered region was revealed after lithiation cycles, which provides atomic-level insight in understanding the cycling behaviors of cathode particles.¹¹³

Electronic structural analysis

Electronic structures, including valence state, bonding conditions, and molecular orbital, can potentially govern the performances of energy and environmental materials. As to transition metal-based materials, for example, the d-band center position relative to the Fermi level is widely accepted as a key descriptor of catalytic activity. Shifting the d-band center upward leads to an increased fraction of unoccupied antibonding states above the Fermi level, resulting in an enhanced absorbing strength of intermediates, and vice versa.^{114,115}

Energy loss near-edge structure (ELNES), a fine structure located in the energy range of about 30 eV above the absorption edge energy in the EELS core-loss spectrum, is a practical method to acquire the electronic structures of materials. It originates from an electron transition from a core orbital to unoccupied states, and reflects the atomic environment, such as bonding conditions, valence states, and orbital information of materials. Compared with X-ray absorption near-edge structure (XANES) spectroscopy, ELNES, combined with STEM, takes advantage of providing local electronic structure with atomic spatial resolution, as discussed below.^{116,117}

Bonding analysis. A remarkable ability of ELNES is to determine the electronic structures of light elements. This is of great significance in characterizing carbon materials that have extensive applications in battery electrodes and catalysis. Ortiz-Medina et al. synthesized ultrathin nanostructured carbon (NC)-based film by plasma-assisted magnetron sputtering technique to desalinate seawater.¹¹⁸ ELNES has been employed to investigate the effect of sputtering gases on the chemical bonding conditions in deposited films. As shown in Figure 11A, the ELNES spectra revealed that CH₄ in the sputtering gas led to a significant increase in the σ* signal, while the addition of N₂ sharpened the π* region. Furthermore, quantitative analysis shows the ratio of (sp³(100)/(sp²+sp³). The addition of N₂ decreases the relative ratio, which is caused by the preferential formation of C=N bonds. On the other hand, the addition of Ar increased this ratio due to the formation of C-N bonds. This technique helped to design an NC film with a 96% salt rejection rate in a 0.2 wt % NaCl solution. Similar analysis can be used in distinguishing diamond and graphite, which cannot be achieved by using EDS due to its relatively lower energy resolution.^{119,120}

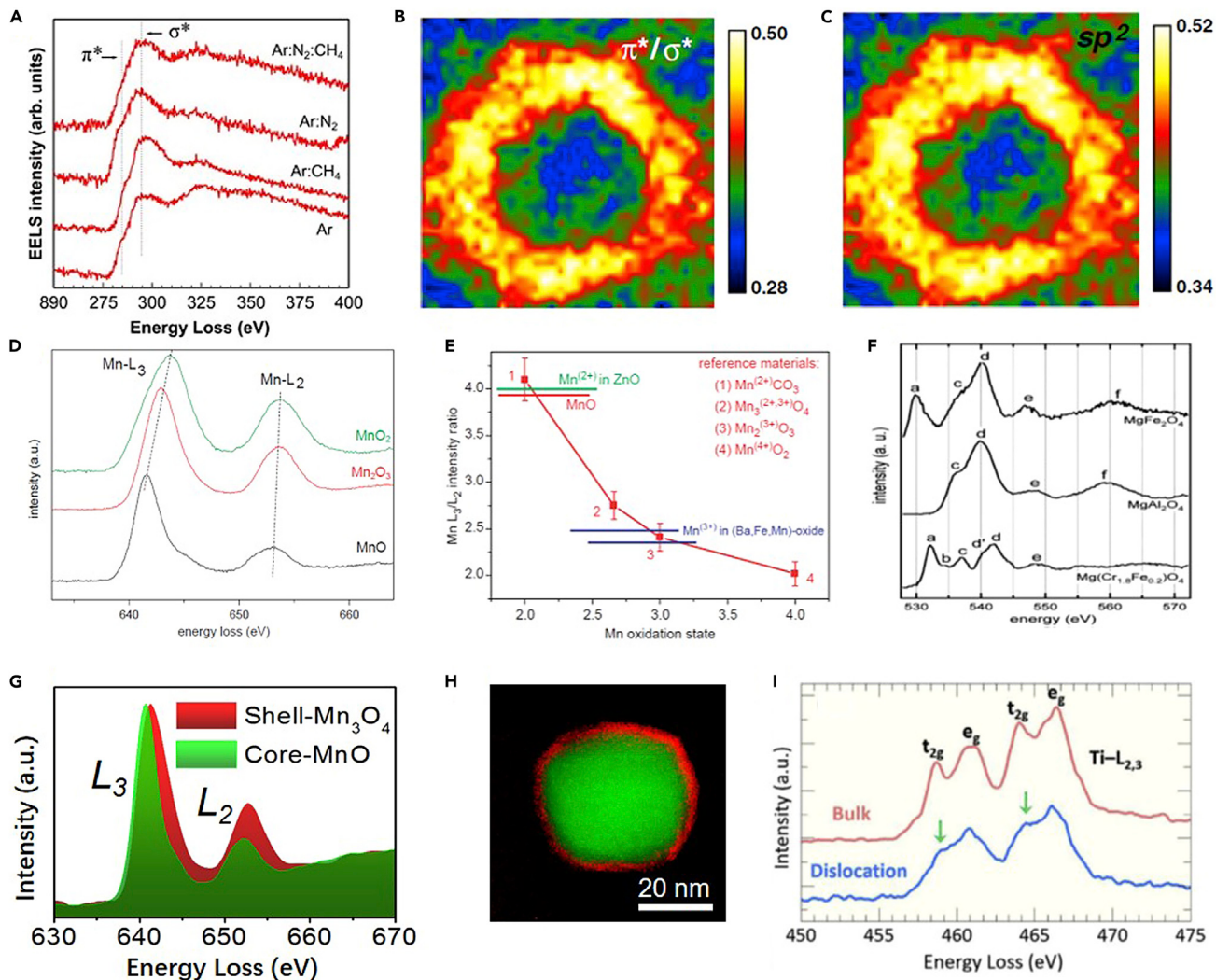


Figure 11. Local electronic structure analysis conducted by EELS

- (A) The EELS in the carbon K-edge region showing the chemical bonding conditions in the deposited carbon film. Reproduced with permission from Ortiz-Medina et al.¹¹⁸ Copyright 2016, Springer Nature.
- (B) Extracted intensity of π^* to σ^* ratio in a functionalized CNT/polymer interface. Reproduced with permission from Su et al.¹²¹ Copyright 2016, Microscopy Society of America.
- (C) Map of sp^2 distribution in functionalized CNT/polymer interface. Reproduced with permission from Su et al.¹²¹ Copyright 2016, Microscopy Society of America.
- (D) Comparison of ELNES Mn-L_{2,3} edges from MnO, Mn₂O₃, and MnO₂.
- (E) Calibration curves showing Mn L₃/L₂ white-line intensity ratio versus Mn oxidation state. Reproduced with permission from Schmid and Mader.¹²² Copyright 2006, Elsevier.
- (F) O-K-edge ELNES of MgFe₂O₄ (inverse spinel), MgAl₂O₄ (normal spinel), and MgFe_{0.2}Cr_{1.8}O₄. Reproduced with permission from Nyquist and Hålenius.¹²³ Copyright 2013, Springer Nature.
- (G) ELNES Mn-L_{2,3} edges and (H) Mn valence states distribution in the nanoparticle, in which Mn from the shell (red) and core (green) were confirmed to be Mn^{II}O and Mn^{II,III}O₄, respectively. Reproduced with permission from Chu et al.¹²⁴ Copyright 2017, WILEY-VCH.
- (I) The Ti-L_{2,3} edge EELS detected at the dislocation core and in the bulk region. Reproduced with permission from Sun et al.¹²⁵ The Royal Society of Chemistry.

The visualization of the bonding conditions of carbon materials in the atomic scale can be conducted by using ELNES-STEM. Su et al. employed ELNES-STEM to observe the bonding conditions on the interfaces of nonfunctionalized and functionalized CNT/polymer nanocomposites.¹²¹ They found that both the sp^2 bonding fraction and the π^*/σ^* ratio in the functionalized CNT/polymer interface are lower than

that in the nonfunctionalized cases (Figures 11B and 11C). So far, STEM-EELS is considered to be one of the few important methods to present a visual correlation between the electronic structure and microstructure down to the atomic level.

Valence state analysis. The electron transitions of $2p^{3/2} \rightarrow 3d^{3/2}3d^{5/2}$ and $2p^{1/2} \rightarrow 3d^{3/2}$ in 3d transition metal leads to the L_3 and L_2 lines in ELNES, which are also called the white lines.¹²⁶ The information of valence state can be extracted by calculating the edge intensity ratio of L_3/L_2 and resolving the edge threshold.¹²² For example, along with the lowering of the oxidation state, the white lines of MnO_2 , Mn_2O_3 , and MnO show a decreasing edge threshold (Figure 11D). Likewise, the L_3/L_2 intensity ratios of $\text{Mn}^{(2+)}\text{CO}_3$, $\text{Mn}^{(2+,3+)}\text{O}_4$, $\text{Mn}_2^{(3+)}\text{O}_3$, and $\text{Mn}^{(4+)}\text{O}_2$ decrease with the increase of the Mn valence state (Figure 11E). Although this trend may differ with other 3d transition metals due to the difference in electron numbers, this method provides a direct way to determine the valence state of 3d transition metals.^{127,128}

Also, the oxygen K-edge is sensitive to the coordination of the surrounding metals, and can be used to reveal the metal valence state.¹²⁹ Nyquist and Hålenius studied the oxygen K-edge ELNES of aluminate, ferrite, and chromate spinels (Figure 11F), and found that the optical absorption coefficient depends on the hybridization between oxygen p-orbitals and metal orbitals in the octahedral coordination field.¹²³ Furthermore, combined with the high spatial resolution of STEM, EELS can be used to map the valence state of transition metals. Our group synthesized $\text{MnO}@\text{Mn}_3\text{O}_4$ core@shell nanoparticles dispersed in N-doped carbon frameworks for the electrode of lithium-ion batteries.¹²⁴ With regard to the EELS point study, Figure 11G shows that the valence states of Mn differ from the core to the shell of the nanoparticle. By calculating the L_3/L_2 intensity ratios, the valence state of Mn was confirmed to be $\text{Mn}^{(+2)}\text{O}$ in the core and $\text{Mn}^{(+2,+3)}\text{O}_4$ in the shell. The 2D mapping of Mn valence state is shown in Figure 11H. This finding helps to understand the performance of the material as a lithium-ion battery electrode.

Molecular orbital and spin analysis. It is widely accepted that the electronic structure contributes significantly to tuning the performances of energy materials. Recently, e_g (high-energy doubly degenerate states splitting from d-orbitals) filling has been utilized as a descriptor for the catalytic behavior of OER catalysts, particularly in transition metal-based perovskites. For perovskites, the e_g orbital is involved in s bonding or σ bonding with surface adsorbates, during which the binding strength is greatly influenced by the e_g orbital occupancy. A stronger binding with oxygen-containing intermediates can be obtained from a lower e_g occupancy.

Using ELNES analysis, not only the valences, but also the e_g filling states in perovskites can be determined. Ikuhara and co-workers studied the ELNES differences of a $\text{Ti-L}_{2,3}$ edge for a region centered at the dislocation core and a bulk-like region.^{125,130} Because of Ti^{3+} near the dislocation core, the relative isotropic distribution of the additional electron is lower than that in the bulk, and results in broader t_{2g} peaks in the Ti-L-edge spectra (Figure 11I). Zhou et al. aim to improve the ORR activity of perovskite cobaltite LaCoO_3 by tuning the e_g filling.¹¹⁵ The increase of the Co e_g filling was achieved from unity to near the optimal configuration of 1.2 by reducing the particle size to ~ 80 nm. The regulation of the electronic structure was verified by analyzing the ELNES spectra of Co L edges and O K edges from the center and edge of the 80- nm nanoparticles.

Current limitations of EELS techniques

In principle, there are alternatives to the above analysis. For example, plasma excitation can be recorded in the optical spectrum, band gap width can be measured from UV photoelectron spectroscopy, and element and valence analysis can be obtained from X-ray photoelectron spectroscopy. However, integrated in TEM, EELS has the unique advantage of ultra-high spatial distribution, which cannot be replaced by other technologies. That is to say, any parameter that EELS can provide can be mapped in two or three dimensions in a local region. Despite this unique advantage, there are some limitations of EELS. The EELS signal-to-background ratio (SBR) decreases as the thickness increases, while the SNR has an optimal value when the thickness is around 0.37λ , here λ is the mean free path of the specimen at corresponding acceleration voltage. That is to say, to acquire good EELS data, the specimen should not be too thick or too thin. A specimen that is too thick leads to low SBR and SNR, and if it is too thin the specimen leads to poor SNR of EELS signal. Alternatively, EELS from thicker specimens can be deconvolved by using the low-loss part of the EELS spectrum, which, however, decreases the SNR of the spectrum.

Due to the significantly higher energy resolution compared with EDS, EELS provides more detailed information in the fine structure of the ionization edges, as we have discussed previously. Practically, however, the intensity of the ionization edge decreases substantially at higher energy range. One limitation of EELS is to acquire excellent data at high-energy range, especially at a range higher than ~ 2 keV. Recently, MacLaren and co-workers succeeded in extending the useful range for quantitative EELS out to at least 5 keV by adjusting the optical path of the electrons.¹³¹ However, this involves complex instrument modifications, which is not practical for ordinary EELS users. Even when using a standard commercial EELS spectrometer, it is necessary to set various parameters according to specific specimens, such as collection angle, convergence angle, camera length, etc., requiring users to have a wealth of knowledge and experience of EELS.

Even for the collected EELS data, correctly analyzing it to extract accurate information is a process that requires knowledge and experience of EELS. For example, in the calculation of the element ratio, it is necessary to subtract the background manually, which is directly related to the experience of the operator. Another example, when using EELS for valence analysis, it is crucial to select an appropriate calculation model. In some cases, one even needs to perform comparative analysis after fitting the EELS spectrum. This largely limits the application of EELS for new learners.

IN SITU TEM TECHNIQUES

Seeing is believing. Using an *in situ* TEM technique, researchers can observe the evolution of materials in various fields, gaseous, and liquid environments at the microscopic scale. As mentioned above, HRTEM and STEM are the most typical imaging modes of TEM. With the rapidly expanding interest in the area of energy conversion devices, such as rechargeable ion cells, fuel cells, and water-splitting electrolyzers, it is of great importance to directly detect real-time chemical reactions, material conversion, and charge flows in these devices. An *in situ* experiment is realized by subjecting the sample to appropriate stimuli, such as heating, electrical biasing, and light, or to specific environments, such as liquid and gas, and then probing the structure evolution or properties changes in real time. In some cases, multiple functionalities have to be integrated in one holder. For example, to conduct an *in situ* study on electrodes of alkali air batteries, a holder that combines electrical biasing and gaseous environment is desired. This section describes the latest

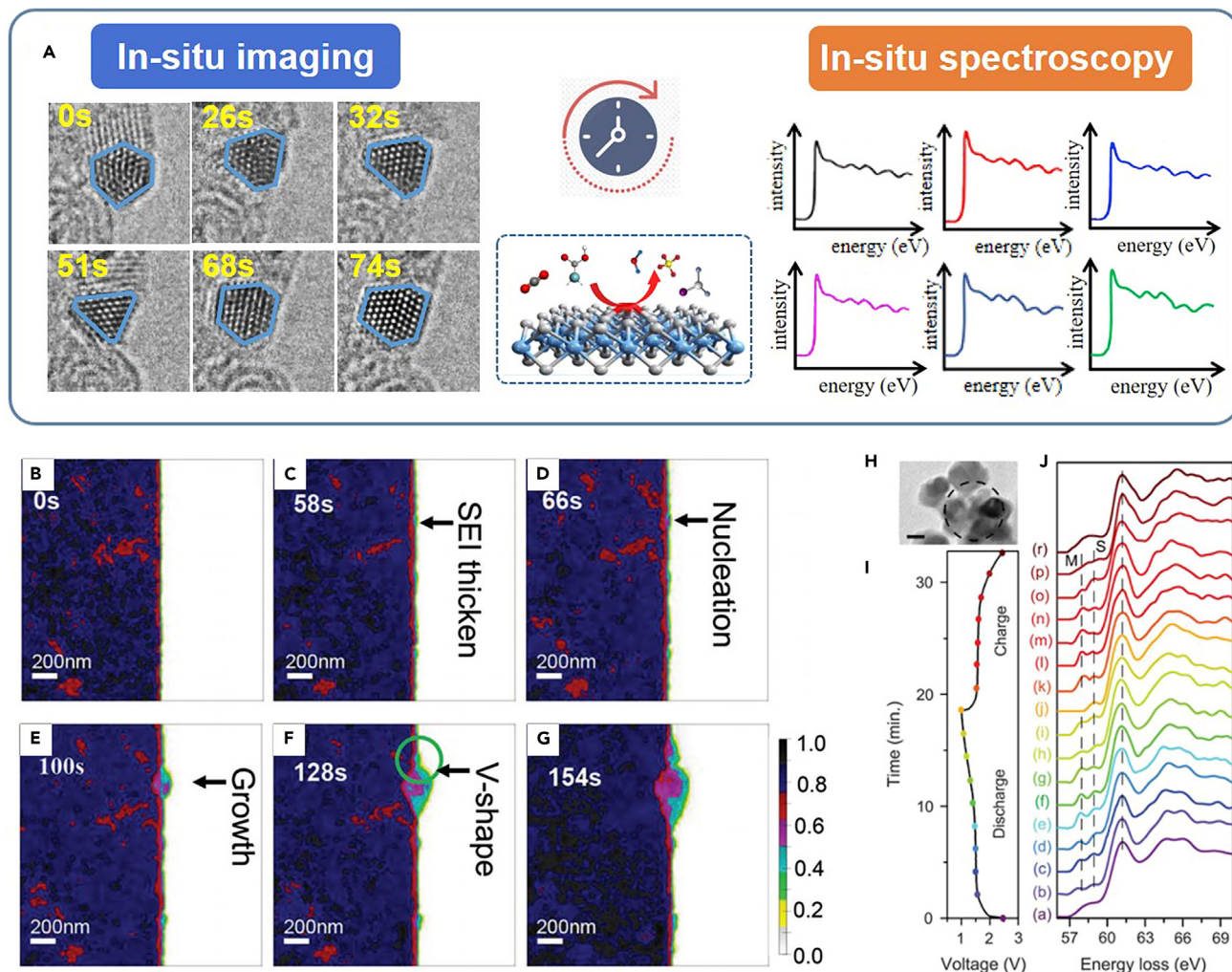


Figure 12. *In situ* TEM techniques

(A) Schematic illustration of *in situ* TEM imaging and spectroscopy.

(B–G) *In-situ* ABF-STEM images of Li lithiation process. The weak contrast of the light SEI was enhanced by colour. Reproduced with permission from Hou et al.¹³² Copyright 2019, Wiley-VCH.

(H) Bright-field TEM image of the LTO nanoparticles selected for EELS measurement. Scale bar, 50 nm.

(I) Voltage applied on the LTO nanoparticles vs time. (J) The sequential EELS spectra corresponding to voltage applied in (I).¹³³ Copyright 2020, The American Association for the Advancement of Science.

development and application of *in situ* techniques for emerging materials, including *in situ* resolving techniques and *in situ* spectroscopic techniques (Figure 12A).

As discussed above, a key challenge to achieve *in situ* TEM observation is to construct various holders with designed functionalities. With regard to heating, a resistance wire is used originally to provide the heat source. However, the thermal shift and vibration greatly influence the stability and thus resolution of the sample. With the development of microelectromechanical systems (MEMS) technology, MEMS with embedded heating units has been adopted, such as the spiral heating unit around observation windows. The micro-heater based on MEMS has merits of heat stability, tiny sample drift, accurate temperature control, and compatibility with spectroscopic techniques, such as EDS.¹³⁴ In addition, the electric field could also be realized using the MEMS chip patterned with electrical circuitry and

microelectrodes. Besides MEMS, another method to apply electrical bias is using an individual tungsten needle or nanowire as electrode and the piezo-positioner to contact the electrode with a sample installed on a TEM-scanning tunneling microscope (STM) holder, which is generally used to investigate the intercalation and de-intercalation processes in rechargeable ion batteries. *In situ* mechanical testing could also be conducted through the TEM-STM holder or more detailed mechanical properties, depending on a micromechanical platform integrated in the TEM holder. Moreover, the light field could be brought in by addition of a light-fiber or light-emitting diode light in the TEM holder to the study of behavior under light excitation.¹³⁵

In addition to these applied fields, gaseous and liquid environments around samples are also created in TEM. Compared with the stimuli holders, it is more difficult to provide proper reaction environments in holders. This is due to the interactions between the electron beam and environmental media that damage the spatial/energy resolutions of the instrument. There are two solutions to introduce gases into the high vacuum of a TEM instrument: environmental TEM (ETEM) and microfabricated gas cells. In ETEM, a differential pump system is fabricated to allow a gas environment around the sample areas, while keeping a low pressure in the electron source. ETEM is convenient to combine with other *in situ* holders, such as heating, cooling, and biasing, but the gas pressure in ETEM is usually low to keep a high vacuum. The gas cell strategy is achieved by sealing two MEMS chips (top and bottom) with electron transparent SiN_x or graphene membrane as imaging windows, with a controlled gas medium surrounding a sample flow between the two chips to isolate the specimen and gas environment from vacuum system. The gas pressure could reach to ambient pressure, and thus closer to real reaction conditions. By incorporating a micro-heating unit on the bottom or top chips, real-time tracking of the gas-solid reaction and dynamic evolution of interface structure were achieved. Furthermore, an *in situ* gas holder equipped with a mass spectrometer enabled on-line detection of product gas species after chemical reactions in TEM, which provided the possibility to relate structure transition with catalytic performance.¹³⁶ A liquid environment was achieved through the liquid cell TEM holder relying on the same MEMS-based chips. The *in situ* liquid technology facilitates achievements in real-time observation and understanding of nucleation and growth of colloidal nanoparticles.¹³⁷ Moreover, through integration of the electrode system in MEMS chips, operando electrochemical measurement within the liquid cell is achievable.¹³⁸ These advanced *in situ* TEM technologies open up a new avenue for cognition about physical and chemical phenomena and the structure-function relationship.

***In situ* resolving techniques**

A remarkable advantage for HRTEM is the rapid imaging process, which is suitable for *in situ* experiments. Thus, the structural evolution of the electrode materials in lithium-ion batteries can be directly observed during the reaction process. Lee et al. studied the lithiation mechanism of MnO₂ nanowires using *in situ* TEM, and determined the fastest lithium-ion diffusion path of cryptopotassium-brucite tunnel nanowires.¹³⁹ By using an open cell *in situ* TEM holder, they successfully detected the optimal lithium-ion diffusion path in the nanowires.¹⁴⁰ In addition, Mai et al. confirmed that Zn₂SiO₄ underwent a transformation and alloying reaction in the lithium process by *in situ* TEM. Zn₂SiO₄ nanowires coated by carbon shells had lower radical expansion and faster reaction kinetics than pure Zn₂SiO₄ nanowires.¹⁴¹

The versatility of STEM also brings unique functionality for *in situ* imaging. For instance, *in situ* ABF-STEM, with the ability to trace light elements, enables the

visualization of the SEI film evolution. Chen's group performed operando observations of SEI films by ABF-STEM to reveal the kinetic evolution of the organic and inorganic layers.¹³² As shown in Figure 12B, a polycrystalline structure of the gold electrode was discovered in the ABF-STEM images. The SEI film displayed a variable thickness, correlated with the heterogeneous nucleation and growth of Li-Au phases (Figures 12C and 12D). ABF-STEM revealed that the lithiation process began with the formation of a Li-Au domain (Figure 12E). A V-shaped area formed at the Li-Au nucleation site due to the large local volume expansion (Figures 12F and 12G). The electrochemical behavior of other electrode materials, such as red phosphorus for sodium-ion batteries, was also surveyed by *in situ* STEM, providing strategies for interface engineering to avoid adverse effects for batteries.¹⁴²

In situ STEM has also been used to probe the structural evolution of the catalyst in different reaction conditions. Yin et al. used *in situ* STEM with a heating holder to track the morphological changes of Pt₃Co/C annealed at 750°C.¹⁴³ More chemical environments are expected to be constructed to investigate the structural evolution of the catalysts in more complex catalytic processes.

***In situ* EELS**

In addition to seeing the evolution of the material's morphology and atomic structure, researchers are also concerned about the material's element distribution and valence changes. This is of great significance for revealing the mechanism of emerging advanced materials during operation. EELS has been employed to determine the electronic structure and chemical properties of specimens. The combination of *in situ* STEM and EELS takes advantage of high spatial resolution and real-time monitoring of electronic structure.

In situ EELS can be used to determine the atomic configuration of metastable intermediate (Li_{4+x}Ti₅O₁₂, LTO) and the related lithium ion transport pathway. Wang's group conducted *in situ* EELS studies to track the lithium-ion migration in real time.¹³³ LTO nanoparticles (Figure 12H) and voltage distributions at different periods (Figure 12I) are presented in the TEM images, and corresponding EELS spectra were then taken at 120 s intervals in the first cycle (Figure 12J). A new peak was found at 58.0 eV, which was not detected in the *ex situ* measurements. The evolution of Li-EELS spectra indicates the occupation and migration of Li, providing key information about rate-dependent behavior.

Current limitations of *in situ* TEM techniques

Usually, we hope to eliminate the effect of the electron beam when studying the intrinsic properties of emerging materials. However, in the *in situ* TEM protocols, the effect of the electron beam cannot be completely avoided. At present, control experiments are usually carried out to show whether the electron beam has a severe effect on the *in situ* process. Sometimes, low-dose imaging is adopted to minimize the effect of the electron beam. In addition, since *in situ* TEM process is usually observed in a local region, it is debatable whether the observed *in situ* mechanism represents the mechanism of the entire specimen. Moreover, whether the mass migration and reaction process in *in situ* TEM are the same as the actual working process is also worthy of attention.

When the *in situ* reaction is carried out in the vacuum of the TEM, which differs from the usual atmospheric environment, in principle, it may cause the *in situ* TEM process to be different from the real situation. The utilization of ETEM enables *in situ* imaging of the specimen in the controlled gaseous environment, almost without loss of

spatial resolution. However, the currently achievable pressure cannot reach that of the atmospheric environment. If windowed gas cells are used, the pressure can reach atmospheric pressure or higher, but the spatial resolution will be reduced due to the electron beam scattering by cells. When imaging specimen in liquid cells, electron beam scattering caused by both the cells and the liquid further reduce the spatial resolution. Sometimes, the complex interaction between the electron beam and the liquid may affect the *in situ* reaction process. These limitations hinder the application of *in situ* TEM, and need to be further resolved.

CONCLUSIONS AND PERSPECTIVES

In this review, we summarize the recent progress in analytical TEM techniques in emerging materials, focusing in particular on the brief principles and practical examples of advanced STEM resolving and derived techniques, including STEM-related data processing, EELS, and *in situ* techniques. Advice on how to utilize advanced TEM techniques to solve the problem in the research of emerging materials has been provided. For instance, HAADF-STEM is suggested for phase identification, heterointerface characterization, defect, and dopant studies. ABF, eABF, and iDPC-STEM techniques are advised for use in light element imaging, such as lithium or oxygen in lithium batteries, or hydrogen in hydrogen storage materials. iDPC-STEM is suggested in electron beam-sensitive materials imaging. Various data-processing techniques, EELS techniques, and *in situ* TEM techniques are advised on corresponding utilization.

Despite the current utilization of analytical TEM technique, there are existing techniques to be extensively utilized. For example, the measurement of 3D dopants at the atomic scale has been realized through HAADF-STEM. This technique is expected to be applied to reveal the relationship between the atomic position of dopants and the resulting performance in emerging materials. Also, the recently developed 4D STEM technique shows potential applications in energy and environmental materials.¹⁴⁴ In the case of nano beam ED, 4D STEM can be conducted to do orientation mapping, like electron backscatter diffraction in scanning electron microscopy, but with significantly higher spatial resolution. Also, Strain mapping can be produced using 4D STEM, and achieved higher accuracy than GPA. Taking these advantages, 4D STEM demonstrates a promising prospect in characterization of emerging materials in the future.

We expect that the future development of TEM would be faster in hardware and smarter in software.

Faster hardware

The acquisition of TEM data, including light element imaging, electron beam-sensitive materials, EDS, and EELS, is greatly limited by the acquisition efficiency of CCD or detector hardware. To gain more insights into energy and environmental materials, more TEM-related techniques are expected to be further developed. One of them is the application of extended energy loss fine structure (EXELFS) of EELS. Analogous to X-ray absorption fine structure spectroscopy, EXELFS oscillations generally start at 40–50 eV above threshold and extend to 200–300 eV above the ELNES region.¹⁴⁵ It is hopeful to offer additional information about materials, such as distribution of near-neighboring atoms of the excited atom, determination of element-specific bond lengths, coordination numbers, coordinating species, and their dynamics process. What's more, the electron beam spot of TEM can be focused to sub-Å scale, offering ultra-high spatial resolution of EXELFS.¹⁴⁵ However, the

application of EXELFS suffers from relatively weak signal and an immature analysis method. To solve this problem, researchers used direct detection electron-counting cameras (K2) to conduct EXELFS-related researches and have demonstrated the potential application of EXELFS.¹⁴⁶ Further improvements are needed to target the practical utilization of this technique.

Smarter software

Considering the applications of big data analysis, artificial intelligence, or machine learning technique,^{147,148} advanced analytical TEM is expected to be smarter. Such breakthroughs will provide new opportunities for the applications of advanced analytical TEM to new materials. What's more, *in situ* TEM is expected to play more important roles in the study of energy and environmental materials. At present, TEM data acquisition relies heavily on the TEM researcher's knowledge and experience. With the development of big data analysis and artificial intelligence, it is expected that computers will acquire high-quality TEM data by themselves, without or with only a small amount of manual intervention. Especially in the processing of massive *in situ* data, computers are expected to automatically identify and extract valid data, and automatically provide suggestions for experimental improvements. If the hardware speed can be guaranteed, TEM imaging, and CBED, EELS, and EDS of specific specimens can be packaged into a single database, which is suitable for comprehensive and multi-angle research. However, due to the diversity of TEM data, achieving this goal requires the collaboration of TEM, materials, and computer researchers.

Also, *in situ* TEM is expected to play more important roles in the study of energy and environmental materials. The time resolution will be increased on capturing images and spectra, showing more details of the process of energy storage and conversion. Multi-dimensional *in situ* conditions and lower electron beam dose need to be applied in *in situ* TEM observation.

ACKNOWLEDGMENTS

The authors give thanks for financial support from the Youth Innovation Promotion Association of CAS (2020458), the National Key Research and Development Program of China (2019YFA0307900), the National Natural Science Foundation of China (11874334), the Collaborative Innovation Program of Hefei Science Center of CAS (2020HSC-CIP013), the State Key Laboratory of Advanced Technology for Materials Synthesis and Processing (WUT, 2021-KF-17), funding from the National Synchrotron Radiation Laboratory (KY2340000115), the Fundamental Research Funds for the Central Universities (grant WK2060190103), and the Natural Science Foundation of Jiangsu Province (no. BK20191443).

AUTHOR CONTRIBUTIONS

Conceptualization, Y.L.; writing – original draft, M.Z., H.L., and Y.L.; writing – review & editing, X.T., H.L., X.H., M.Z., Y.L., and J.Y.; visualization, X.T. and X.H.; supervision, Y.L.

DECLARATION OF INTERESTS

The authors declare no competing interests.

REFERENCES

- Li, M., Lu, J., Chen, Z., and Amine, K. (2018). 30 years of lithium-ion batteries. *Adv. Mater.* 30, e1800561.
- Ji, B., Yao, W., Zheng, Y., Kidkhunthod, P., Zhou, X., Tunmee, S., Sattayaporn, S., Cheng, H.-M., He, H., and Tang, Y. (2020). A fluoroxalate cathode material for potassium-ion batteries with ultra-long cyclability. *Nat. Commun.* 11, 1225.

3. Nayak, P.K., Yang, L., Brehm, W., and Adelhelm, P. (2018). From lithium-ion to sodium-ion batteries: advantages, challenges, and surprises. *Angew. Chem. Int. Ed.* 57, 102–120.
4. Lu, F., Zhou, M., Li, W.-R., Weng, Q.-H., Li, C.-L., Xue, Y.-M., Jiang, X.-F., Zeng, X.-H., Bando, Y., and Golberg, D. (2016). Engineering sulfur vacancies and impurities in NiCo₂S₄ nanostructures toward optimal supercapacitive performance. *Nano Energy* 26, 313–323.
5. Raza, W., Ali, F., Raza, N., Luo, Y., Kim, K.-H., Yang, J., Kumar, S., Mehmood, A., and Kwon, E.E. (2018). Recent advancements in supercapacitor technology. *Nano Energy* 52, 441–473.
6. Werner, J., Weng, C.H., Walter, A., Fesquet, L., Seif, J.P., De Wolf, S., Niesen, B., and Ballif, C. (2016). Efficient monolithic perovskite/silicon tandem solar cell with cell area >1 cm². *J. Phys. Chem. Lett.* 7, 161–166.
7. Yoshikawa, K., Kawasaki, H., Yoshida, W., Irie, T., Konishi, K., Nakano, K., Uto, T., Adachi, D., Kanematsu, M., Uzu, H., et al. (2017). Silicon heterojunction solar cell with interdigitated back contacts for a photoconversion efficiency over 26%. *Nat. Energy* 2, 17032.
8. Mustain, W.E., Chatenet, M., Page, M., and Kim, Y.S. (2020). Durability challenges of anion exchange membrane fuel cells. *Energy Environ. Sci.* 13, 2805–2838.
9. Li, M., Bi, X.-X., Wang, R.-Y., Li, Y.-B., Jiang, G.-P., Li, L., Zhong, C., Chen, Z.-W., and Lu, J. (2020). Relating catalysis between fuel cell and metal-air batteries. *Matter* 2, 32–49.
10. Huang, Y., Wang, Y., Tang, C., Wang, J., Zhang, Q., Wang, Y., and Zhang, J. (2019). Atomic modulation and structure design of carbons for bifunctional electrocatalysis in metal-air batteries. *Adv. Mater.* 31, e1803800.
11. Jung, E., Shin, H., Lee, B.H., Efremov, V., Lee, S., Lee, H.S., Kim, J., Hooch Antink, W., Park, S., Lee, K.S., et al. (2020). Atomic-level tuning of Co-N-C catalyst for high-performance electrochemical H₂O₂ production. *Nat. Mater.* 19, 436–442.
12. Wan, C.-Z., Duan, X.-F., and Huang, Y. (2020). Molecular design of single-atom catalysts for oxygen reduction reaction. *Adv. Energy Mater.* 10, 1903815.
13. Tian, W., Zhang, S., Huo, C., Zhu, D., Li, Q., Wang, L., Ren, X., Xie, L., Guo, S., Chu, P.-K., et al. (2018). Few-layer antimonene: anisotropic expansion and reversible crystalline-phase evolution enable large-capacity and long-life Na-ion batteries. *ACS Nano* 12, 1887–1893.
14. Fang, G.-Z., Zhu, C.-Y., Chen, M.-H., Zhou, J., Tang, B., Cao, X.-X., Zheng, X.-S., Pan, A.-Q., and Liang, S.-Q. (2019). Suppressing manganese dissolution in potassium manganate with rich oxygen defects engaged high-energy-density and durable aqueous zinc-ion battery. *Adv. Funct. Mater.* 29, 1808375.
15. Yang, J., Yu, C., Fan, X.-M., Liang, S.-X., Li, S.-F., Huang, H.-W., Ling, Z., Hao, C., and Qiu, J.-S. (2016). Electroactive edge site-enriched nickel-cobalt sulfide into graphene frameworks for high-performance asymmetric supercapacitors. *Energy Environ. Sci.* 9, 1299–1307.
16. Jiang, Y., Chen, Z., Han, Y., Deb, P., Gao, H., Xie, S., Purohit, P., Tate, M.W., Park, J., Gruner, S.M., et al. (2018). Electron ptychography of 2D materials to deep sub-Ångström resolution. *Nature* 559, 343–349.
17. Fan, Z., Zhang, L., Baumann, D., Mei, L., Yao, Y., Duan, X., Shi, Y., Huang, J., Huang, Y., and Duan, X. (2019). In situ transmission electron microscopy for energy materials and devices. *Adv. Mater.* 31, e1900608.
18. Zhang, C., Firestein, K.L., Fernando, J.F.S., Siriwardena, D., von Treifeldt, J.E., and Golberg, D. (2020). Recent progress of in situ transmission electron microscopy for energy materials. *Adv. Mater.* 32, e1904094.
19. Su, D. (2017). Advanced electron microscopy characterization of nanomaterials for catalysis. *Green. Energy Environ* 2, 70–83.
20. MacLaren, I., and Ramasse, Q.M. (2014). Aberration-corrected scanning transmission electron microscopy for atomic-resolution studies of functional oxides. *Int. Mater. Rev.* 59, 115–131.
21. Saghi, Z., and Midgley, P.A. (2012). Electron tomography in the (S)TEM: from nanoscale morphological analysis to 3D atomic imaging. *Annu. Rev. Mater. Res.* 42, 59–79.
22. LeBeau, J.M., Findlay, S.D., Allen, L.J., and Stemmer, S. (2010). Standardless atom counting in scanning transmission electron microscopy. *Nano Lett.* 10, 4405–4408.
23. Gao, P., Ishikawa, R., Tochigi, E., Kumamoto, A., Shibata, N., and Ikuhara, Y. (2017). Atomic-scale tracking of a phase transition from spinel to rocksalt in lithium manganese oxide. *Chem. Mater.* 29, 1006–1013.
24. Bu, L.-Z., Zhang, N., Guo, S.-J., Zhang, X., Li, J., Yao, J.-L., Wu, T., Lu, G., Ma, J.-Y., Su, D., et al. (2016). Biaxially strained PtPb/Pt core/shell nanoplate boosts oxygen reduction catalysis. *Science* 354, 1410–1414.
25. Zhang, L., Jia, Y., Gao, G., Yan, X., Chen, N., Chen, J., et al. (2018). Graphene Defects Trap Atomic Ni Species for Hydrogen and Oxygen Evolution Reactions. *Chem* 4, 285–297.
26. Krivanek, O.L., Chisholm, M.F., Nicolosi, V., Pennycook, T.J., Corbin, G.J., Dellby, N., Murfitt, M.F., Own, C.S., Szilagyi, Z.S., Oxley, M.P., et al. (2010). Atom-by-atom structural and chemical analysis by annular dark-field electron microscopy. *Nature* 464, 571–574.
27. Feng, S., Song, X., Liu, Y., Lin, X., Yan, L., Liu, S., Dong, W., Yang, X., Jiang, Z., and Ding, Y. (2019). In situ formation of mononuclear complexes by reaction-induced atomic dispersion of supported noble metal nanoparticles. *Nat. Commun.* 10, 5281.
28. Lu, F., Yi, D., Liu, S., Zhan, F., Zhou, B., Gu, L., Golberg, D., Wang, X., and Yao, J. (2020). Engineering platinum-oxygen dual catalytic sites via charge transfer towards high-efficient hydrogen evolution. *Angew. Chem. Int. Ed.* 132, 17865–17871.
29. Zhao, S.-Y., Chen, G.-X., Zhou, G.-M., Yin, L.-C., Veder, J.P., Johannessen, B., Saunders, M., Yang, S.-Z., De Marco, R., Liu, C., et al. (2019). A universal seeding strategy to synthesize single atom catalysts on 2D materials for electrocatalytic applications. *Adv. Funct. Mater.* 30, 1906157.
30. Liu, G., Robertson, A.W., Li, M.M., Kuo, W.C.H., Darby, M.T., Muhammedine, M.H., Lin, Y.C., Suenaga, K., Stamatakis, M., Warner, J.H., et al. (2017). MoS₂ monolayer catalyst doped with isolated Co atoms for the hydrodeoxygenation reaction. *Nat. Chem.* 9, 810–816.
31. Harrach, H.S.v., Dona, P., Freitag, B., Soltau, H., Niculae, A., and Rohde, M. (2009). An integrated silicon drift detector system for FEI Schottky field emission transmission electron microscopes. *Microsc. Microanal.* 15, 208–209.
32. Findlay, S.D., Shibata, N., Sawada, H., Okunishi, E., Kondo, Y., Yamamoto, T., and Ikuhara, Y. (2009). Robust atomic resolution imaging of light elements using scanning transmission electron microscopy. *Appl. Phys. Lett.* 95, 191913.
33. Wen, Y., Shang, T., and Gu, L. (2017). Analytical ABF-STEM imaging of Li ions in rechargeable batteries. *Microscopy (Oxf)* 66, 25–38.
34. Ji, Y.-R., Weng, S.-T., Li, X.-Y., Zhang, Q.-H., and Gu, L. (2020). Atomic-scale structural evolution of electrode materials in Li-ion batteries: a review. *Rare Met.* 39, 205–217.
35. Okunishi, E., Sawada, H., and Kondo, Y. (2012). Experimental study of annular bright field (ABF) imaging using aberration-corrected scanning transmission electron microscopy (STEM). *Micron* 43, 538–544.
36. Gong, Y., Zhang, J., Jiang, L., Shi, J.-A., Zhang, Q., Yang, Z., Zou, D., Wang, J., Yu, X., Xiao, R., et al. (2017). In situ atomic-scale observation of electrochemical delithiation induced structure evolution of LiCoO₂ cathode in a working all-solid-state battery. *J. Am. Chem. Soc.* 139, 4274–4277.
37. Xiao, Y., Zhu, Y.-F., Yao, H.-R., Wang, P.-F., Zhang, X.-D., Li, H.-L., Yang, X., Gu, L., Li, Y.-C., Wang, T., et al. (2019). A stable layered oxide cathode material for high-performance sodium-ion battery. *Adv. Energy Mater.* 9, 1803978.
38. Ryu, J., Jang, H., Park, J., Yoo, Y., Park, M., and Cho, J. (2018). Seed-mediated atomic-scale reconstruction of silver manganate nanoparticles for oxygen reduction towards high-energy aluminum-air flow batteries. *Nat. Commun.* 9, 3715.
39. Oshima, Y., Sawada, H., Hosokawa, F., Okunishi, E., Kaneyama, T., Kondo, Y., Niitaka, S., Takagi, H., Tanishiro, Y., and Takayanagi, K. (2010). Direct imaging of lithium atoms in LiV₂O₄ by spherical aberration-corrected electron microscopy. *J. Electron. Microscop. (Tokyo)* 59, 457–461.
40. Gu, L., Zhu, C., Li, H., Yu, Y., Li, C., Tsukimoto, S., Maier, J., and Ikuhara, Y. (2011). Direct observation of lithium staging in partially delithiated LiFePO₄ at atomic resolution. *J. Am. Chem. Soc.* 133, 4661–4663.

41. Shen, B., Chen, X., Shen, K., Xiong, H., and Wei, F. (2020). Imaging the node-linker coordination in the bulk and local structures of metal-organic frameworks. *Nat. Commun.* 11, 2692.
42. Findlay, S.D., Kohno, Y., Cardamone, L.A., Ikuhara, Y., and Shibata, N. (2014). Enhanced light element imaging in atomic resolution scanning transmission electron microscopy. *Ultramicroscopy* 136, 31–41.
43. Graaf, S.D., Momand, J., Mitterbauer, C., Lazar, S., and Kooi, B.J. (2020). Resolving hydrogen atoms at metal-metal hydride interfaces. *Sci. Adv.* 6, 4312.
44. Shen, B., Chen, X., Cai, D., Xiong, H., Liu, X., Meng, C., Han, Y., and Wei, F. (2020). Atomic spatial and temporal imaging of local structures and light elements inside zeolite frameworks. *Adv. Mater.* 32, e1906103.
45. Song, K.-P., Liu, L.-M., Zhang, D.-L., Hautzinger, M.P., Jin, S., and Han, Y. (2020). Atomic-resolution imaging of halide perovskites using electron microscopy. *Adv. Energy Mater.* 10, 1904006.
46. Lazic, I., Bosch, E.G.T., and Lazar, S. (2016). Phase contrast STEM for thin samples: integrated differential phase contrast. *Ultramicroscopy* 160, 265–280.
47. Liu, L., Wang, N., Zhu, C., Liu, X., Zhu, Y., Guo, P., Alfilifi, L., Dong, X., Zhang, D., and Han, Y. (2020). Direct imaging of atomically dispersed molybdenum that enables location of aluminum in the framework of zeolite ZSM-5. *Angew. Chem. Int. Ed.* 59, 819–825.
48. Zhu, Y., Ciston, J., Zheng, B., Miao, X., Czarnik, C., Pan, Y., Sougrat, R., Lai, Z., Hsiung, C.E., Yao, K., et al. (2017). Unravelling surface and interfacial structures of a metal-organic framework by transmission electron microscopy. *Nat. Mater.* 16, 532–536.
49. Zhang, D.-L., Zhu, Y.-H., Liu, L.-M., Ying, X.-G., Hsiung, C.E., Sougrat, R., and Li, K. (2018). Atomic-resolution transmission electron microscopy of electron beam-sensitive crystalline materials. *Science* 359, 675–679.
50. Huang, W., Boyle, D.T., Li, Y., Li, Y., Pei, A., Chen, H., and Cui, Y. (2019). Nanostructural and electrochemical evolution of the solid-electrolyte interphase on CuO nanowires revealed by cryogenic-electron microscopy and impedance spectroscopy. *ACS Nano* 13, 737–744.
51. Wang, H., Li, Y., Li, Y., Liu, Y., Lin, D., Zhu, C., Chen, G., Yang, A., Yan, K., Chen, H., et al. (2019). Wrinkled graphene cages as hosts for high-capacity Li metal anodes shown by cryogenic electron microscopy. *Nano Lett.* 19, 1326–1335.
52. Li, Y.-Z., Li, Y.-B., Pei, A., Yan, K., Sun, Y.-M., Wu, C.-L., Joubert, L.M., Chin, R., Koh, A.L., Yu, Y., et al. (2017). Atomic structure of sensitive battery materials and interfaces revealed by cryo-electron microscopy. *Science* 358, 506–510.
53. Zachman, M.J., Tu, Z., Choudhury, S., Archer, L.A., and Kourkoutis, L.F. (2018). Cryo-STEM mapping of solid-liquid interfaces and dendrites in lithium-metal batteries. *Nature* 560, 345–349.
54. Zhu, Y.-M., Gui, Z.-G., Wang, Q., Meng, F.-X., Feng, S.-H., Han, B., Wang, P.-Y., Huang, L., Wang, H.-L., and Gu, M. (2020). Direct atomic scale characterization of the surface structure and planar defects in the organic-inorganic hybrid $\text{CH}_3\text{NH}_3\text{PbI}_3$ by cryo-TEM. *Nano Energy* 73, 104820.
55. Li, Y.-Z., Wang, K.-C., Zhou, W.-J., Li, Y.-B., Vila, R., Huang, W., Wang, H.-X., Chen, G.-X., Wu, G.-H., Tsao, Y., et al. (2019). Cryo-EM structures of atomic surfaces and host-guest chemistry in metal-organic frameworks. *Matter* 1, 428–438.
56. Arquer, F.P.G., Dinh, C.T., Ozden, A., Wicks, J., McCallum, C., Kirmani, A.R., Nam, D.H., Gabardo, C., Seifitokaldani, A., Wang, X., et al. (2020). CO_2 electrolysis to multicarbon products at activities greater than 1 A cm^{-2} . *Science* 367, 661–666.
57. Allen, F.I., Comolli, L.R., Kusoglu, A., Modestino, M.A., Minor, A.M., and Weber, A.Z. (2014). Morphology of hydrated as-cast nafion revealed through cryo electron tomography. *ACS Macro Lett.* 4, 1–5.
58. Häyter, M.J. (1997). Geometric phase analysis of high resolution electron microscope images. *Scanning Microsc.* 11, 53–66.
59. Häyter, M.J., Snoeck, E., and Kilaas, R. (1998). Quantitative measurement of displacement and strain fields from HREM micrographs. *Ultramicroscopy* 74, 131–146.
60. Nilsson Pingel, T., Jorgensen, M., Yankovich, A.B., Gronbeck, H., and Olsson, E. (2018). Influence of atomic site-specific strain on catalytic activity of supported nanoparticles. *Nat. Commun.* 9, 2722.
61. Gao, P., Liu, H.-J., Huang, Y.-L., Chu, Y.-H., Ishikawa, R., Feng, B., Jiang, Y., Shibata, N., Wang, E.-G., and Ikuhara, Y. (2016). Atomic mechanism of polarization-controlled surface reconstruction in ferroelectric thin films. *Nat. Commun.* 7, 11318.
62. Gan, L., Yu, R., Luo, J., Cheng, Z., and Zhu, J. (2012). Lattice strain distributions in individual dealloyed Pt-Fe catalyst nanoparticles. *J. Phys. Chem. Lett.* 3, 934–938.
63. Mao, J., Chen, W., Sun, W., Chen, Z., Pei, J., He, D., Lv, C., Wang, D., and Li, Y. (2017). Rational control of the selectivity of a ruthenium catalyst for hydrogenation of 4-nitrostyrene by strain regulation. *Angew. Chem. Int. Ed.* 56, 11971–11975.
64. Liang, G.-S., Yang, L.-T., Han, Q., Chen, G.-Y., Lin, C.-F., Chen, Y.-J., Luo, L.-J., Liu, X.-H., Li, Y.-S., and Che, R.-C. (2020). Conductive $\text{Li}_{3.08}\text{Cr}_{0.02}\text{Si}_{0.09}\text{V}_{0.9}\text{O}_4$ anode material: novel “zero-strain” characteristic and superior electrochemical Li^+ storage. *Adv. Energy Mater.* 10, 1904267.
65. Xiao, Y., Wu, H., Li, W., Yin, M., Pei, Y., Zhang, Y., Fu, L., Chen, Y., Pennycook, S.J., Huang, L., et al. (2017). Remarkable roles of Cu to synergistically optimize phonon and carrier transport in n-type $\text{PbTe-Cu}_2\text{Te}$. *J. Am. Chem. Soc.* 139, 18732–18738.
66. Cai, J.-Y., Song, Y., Zhang, Y.-P., Niu, S.-W., Wu, Y.-S., Xie, Y.-F., Zheng, X.-S., Liu, Y., Lin, Y., Liu, X.-J., et al. (2020). N-induced lattice contraction generally boosts the hydrogen evolution catalysis of P-rich metal phosphides. *Sci. Adv.* 6, 8113.
67. Byeon, P., Bae, H.B., Chung, H.-S., Lee, S.-G., Kim, J.-G., Lee, H.J., Choi, J.W., and Chung, S.-Y. (2018). Atomic-scale observation of LiFePO_4 and LiCoO_2 dissolution behavior in aqueous solutions. *Adv. Funct. Mater.* 28, 1804564.
68. Yan, P., Zheng, J., Gu, M., Xiao, J., Zhang, J.-G., and Wang, C.-M. (2017). Intrgranular cracking as a critical barrier for high-voltage usage of layer-structured cathode for lithium-ion batteries. *Nat. Commun.* 8, 14101.
69. Gong, Y., Chen, Y., Zhang, Q., Meng, F., Shi, J.-A., Liu, X., Liu, X., Zhang, J., Wang, H., Wang, J., et al. (2018). Three-dimensional atomic-scale observation of structural evolution of cathode material in a working all-solid-state battery. *Nat. Commun.* 9, 3341.
70. Wu, Y., Cai, J., Xie, Y., Niu, S., Zang, Y., Wu, S., Liu, Y., Lu, Z., Fang, Y., Guan, Y., et al. (2020). Regulating the interfacial electronic coupling of Fe_2N via orbital steering for hydrogen evolution catalysis. *Adv. Mater.* 32, e1904346.
71. Ling, T., Yan, D.-Y., Wang, H., Jiao, Y., Hu, Z., Zheng, Y., Zheng, L., Mao, J., Liu, H., Du, X.W., et al. (2017). Activating cobalt(II) oxide nanorods for efficient electrocatalysis by strain engineering. *Nat. Commun.* 8, 1509.
72. Tinoco, M., Maduro, L., Masaki, M., Okunishi, E., and Conesa-Boj, S. (2017). Strain-dependent edge structures in MoS_2 layers. *Nano Lett.* 17, 7021–7026.
73. Xiong, Y., Shan, H., Zhou, Z., Yan, Y., Chen, W., Yang, Y., Liu, Y., Tian, H., Wu, J., Zhang, H., et al. (2017). Tuning surface structure and strain in Pd-Pt core-shell nanocrystals for enhanced electrocatalytic oxygen reduction. *Small* 13, 1603423.
74. Kret, S., Ruterana, P., Rosenauer, A., and Gerthsen, D. (2001). Extracting quantitative information from high resolution electron microscopy. *Phys. Stat. Sol.* 227, 247–295.
75. Shah, J.K. (2018). Ab initio molecular dynamics simulations of ionic liquids. *Annu. Rep. Comput. Chem.* 95–122.
76. Lang, J., Ding, B., Zhang, S., Su, H., Ge, B., Qi, L., Gao, H., Li, X., Li, Q., and Wu, H. (2017). Scalable synthesis of 2D Si nanosheets. *Adv. Mater.* 29, e1701777.
77. Wu, G., Zheng, X., Cui, P., Jiang, H., Wang, X., Qu, Y., Chen, W., Lin, Y., Li, H., Han, X., et al. (2019). A general synthesis approach for amorphous noble metal nanosheets. *Nat. Commun.* 10, 4855.
78. Gao, W.-P., Tieu, P., Addiego, C., Ma, Y.-L., Wu, J.-B., and Pan, X.-Q. (2019). Probing the dynamics of nanoparticle formation from a precursor at atomic resolution. *Sci. Adv.* 5, 9590.
79. Egami, T., and Billinge, S.J.L. (2012). Chapter 3—the method of total scattering and atomic pair distribution function analysis, underneath Bragg peaks. *Struct. nat. Complex Mater.* 16, 55–111.
80. Fischer, H.E., Barnes, A.C., and Salmon, P.S. (2006). Neutron and X-ray diffraction studies

- of liquids and glasses. *Rep. Prog. Phys.* 69, 233–299.
81. Kilaas, R. (1998). Optimal and near-optimal filters in high-resolution electron microscopy. *J. Microsc.* 190, 45–51.
82. Hou, C.-Y., Zhang, M.-W., Zhang, L.-L., Tang, Y.-Y., Wang, H.-Z., and Chi, Q.-J. (2017). Reagent-free electrophoretic synthesis of few-atom-thick metal oxide nanosheets. *Chem. Mater.* 29, 1439–1446.
83. Ni, B., Wang, K., He, T., Gong, Y., Gu, L., Zhuang, J., and Wang, X. (2018). Mimic the photosystem II for water oxidation in neutral solution: a case of Co_3O_4 . *Adv. Energy Mater.* 8, 1702313.
84. Nairan, A., Zou, P.-C., Liang, C.-W., Liu, J.-X., Wu, D., Liu, P., and Yang, C. (2019). NiMo solid solution nanowire array electrodes for highly efficient hydrogen evolution reaction. *Adv. Funct. Mater.* 29, 1903747.
85. Han, H., Choi, H., Mhin, S., Hong, Y.-R., Kim, K.M., Kwon, J., Ali, G., Chung, K.Y., Je, M., Umh, H.N., et al. (2019). Advantageous crystalline-amorphous phase boundary for enhanced electrochemical water oxidation. *Energy Environ. Sci.* 12, 2443–2454.
86. Jung, K., Lee, J., Kim, Y.-M., Kim, J., Kim, C.-U., and Lee, M.-J. (2016). Influence of defects and nanoscale strain on the photovoltaic properties of CdS/CdSe nanocomposite ZnO nanowire solar cells. *Electro. Acta* 220, 500–510.
87. Ma, T., Wang, S., Chen, M.-D., Maligal-Ganesh, R.V., Wang, L.-L., Johnson, D.D., Kramer, M.J., Huang, W.-Y., and Zhou, L. (2019). Toward phase and catalysis control: tracking the formation of intermetallic nanoparticles at atomic scale. *Chem* 5, 1235–1247.
88. Wu, X.J., Huang, X., Liu, J., Li, H., Yang, J., Li, B., Huang, W., and Zhang, H. (2014). Two-dimensional CuSe nanosheets with microscale lateral size: synthesis and template-assisted phase transformation. *Angew. Chem. Int. Ed.* 53, 5083–5087.
89. Hudak, B.M., Depner, S.W., Waetzig, G.R., Talapatra, A., Arroyave, R., Banerjee, S., and Guiton, B.S. (2017). Real-time atomistic observation of structural phase transformations in individual hafnia nanorods. *Nat. Commun.* 8, 15316.
90. Miao, J., Ercius, P., and Billinge, S.J. (2016). Atomic electron tomography: 3D structures without crystals. *Science* 353, aaf2157.
91. Goris, B., De Beenhouwer, J., De Backer, A., Zanaga, D., Batenburg, K.J., Sanchez-Iglesias, A., Liz-Marzan, L.M., Van Aer, S., Bals, S., Sijbers, J., et al. (2015). Measuring lattice strain in three dimensions through electron microscopy. *Nano Lett.* 15, 69C96–7001.
92. Kim, B.H., Heo, J., Kim, S., Reboul, C.F., Chun, H., Kang, D., Bae, H., Hyun, H., Lim, J., Lee, H., et al. (2020). Critical differences in 3D atomic structure of individual ligand-protected nanocrystals in solution. *Science* 368, 60–67.
93. Zhou, J., Yang, Y., Yang, Y., Kim, D.S., Yuan, A., Tian, X., Ophus, C., Sun, F., Schmid, A.K., Nathanson, M., et al. (2019). Observing crystal nucleation in four dimensions using atomic electron tomography. *Nature* 570, 500–503.
94. Przybilla, T., Zubiri, B.A., Beltrán, A.M., Butz, B., Machoke, A.G.F., Inayat, A., et al. (2018). Transfer of individual micro- and nanoparticles for high-precision 3D analysis using 360° electron tomography. *Small Methods* 2, 1700276-1–1700276-1700277. <https://doi.org/10.1002/smtd.201700276>.
95. Koneti, S., Roiban, L., Dalmas, F., Langlois, C., Gay, A.-S., Cabiac, A., Grenier, T., Banjak, H., Maxim, V., and Epicier, T. (2019). Fast electron tomography: applications to beam sensitive samples and in situ TEM or operando environmental TEM studies. *Mater. Charact.* 151, 480–495.
96. Lovejoy, T.C., Ramasse, Q.M., Falke, M., Kaeppel, A., Terborg, R., Zan, R., et al. (2012). Single atom identification by energy dispersive X-ray spectroscopy. *Appl. Phys. Lett.* 100, 154101-1–154101-154104. <https://doi.org/10.1063/1.3701598>.
97. Hillier, J. (1943). On microanalysis by electrons. *Phys. Rev.* 64, 318–319.
98. Hillier, J., and Baker, R.F. (1944). Microanalysis by means of electrons. *J. Appl. Phys.* 15, 663–675.
99. Krivanek, O.L., Dellby, N., Hachtel, J.A., Idrobo, J.C., Hotz, M.T., Plotkin-Swing, B., Bacon, N.J., Bleloch, A.L., Corbin, G.J., Hoffman, M.V., et al. (2019). Progress in ultrahigh energy resolution EELS. *Ultramicroscopy* 203, 60–67.
100. Idrobo, J.C., and Zhou, W. (2017). A short story of imaging and spectroscopy of two-dimensional materials by scanning transmission electron microscopy. *Ultramicroscopy* 180, 156–162.
101. Long, A., Li, W., Zhou, M., Gao, W., Liu, B., Wei, J., Zhang, X., Liu, H., Liu, Y., and Zeng, X. (2019). MoS₂ nanosheets grown on nickel chalcogenides: controllable synthesis and electrocatalytic origins for the hydrogen evolution reaction in alkaline solution. *J. Mater. Chem. A* 7, 21514.
102. Egerton, R.F. (1996). *Electron Energy-Loss Spectroscopy in the Electron Microscope*, 2nd ed. (New York: Plenum Press).
103. Collins, S.M., Fernandez-Garcia, S., Calvino, J.J., and Midgley, P.A. (2017). Sub-nanometer surface chemistry and orbital hybridization in lanthanum-doped ceria nano-catalysts revealed by 3D electron microscopy. *Sci. Rep.* 7, 5406.
104. Nicoletti, O., de la Pena, F., Leary, R.K., Holland, D.J., Ducati, C., and Midgley, P.A. (2013). Three-dimensional imaging of localized surface plasmon resonances of metal nanoparticles. *Nature* 502, 80–84.
105. Nelayah, J., Kociak, M., Stéphan, O., García de Abajo, F.J., Tencé, M., Henrard, L., Taverna, D., Pastoriza-Santos, I., Liz-Marzáñ, L.M., and Collie, C. (2007). Mapping surface plasmons on a single metallic nanoparticle. *Nat. Phys.* 3, 348–353.
106. Virdi, K.S., Kauffmann, Y., Ziegler, C., Ganter, P., Blaha, P., Lotsch, B.V., Kaplan, W.D., and Scheu, C. (2016). Band gap extraction from individual two-dimensional perovskite nanosheets using valence electron energy loss spectroscopy. *J. Phys. Chem. C* 120, 11170–11179.
107. Zhan, W., Venkatachalapathy, V., Aarholt, T., Kuznetsov, A.Y., and Prytz, O. (2018). Band gap maps beyond the delocalization limit: correlation between optical band gaps and plasmon energies at the nanoscale. *Sci. Rep.* 8, 848.
108. Deitz, J.I., Paul, P.K., Farshchi, R., Poplavskyy, D., Bailey, J., Arehart, A.R., McComb, D.W., and Grassman, T.J. (2019). Direct nanoscale characterization of deep levels in AgCuInGaSe₂ using electron energy-loss spectroscopy in the scanning transmission electron microscope. *Adv. Energy Mater.* 9, 1901612.
109. Wang, S., March, K., Ponce, F.A., and Rez, P. (2019). Identification of point defects using high-resolution electron energy loss spectroscopy. *Phys. Rev. B* 99, 115312.
110. Chung, H.T., Cullen, D.A., Higgins, D., Sneed, B.T., Holby, E.F., More, K.L., and Zelenay, P. (2017). Direct atomic-level insight into the active sites of a high-performance PGM-free ORR catalyst. *Science* 357, 479–484.
111. Yang, Y., Xiong, Y., Holtz, M.E., Feng, X., Zeng, R., Chen, G., DiSalvo, F.J., Muller, D.A., and Abruna, H.D. (2019). Octahedral spinel electrocatalysts for alkaline fuel cells. *Proc. Natl. Acad. Sci. U S A* 116, 24425–24432.
112. Cosandey, F., Marandian Hagh, N., and Amatucci, G.G. (2009). EELS and HRTEM Analysis of Surface Phase in Nanostructured LiMn1.5Ni0.5O4 Battery Materials. *Microsc. Microanal.* 15, 1396–1397.
113. Yan, P., Zheng, J., Zhang, J.G., and Wang, C. (2017). Atomic resolution structural and chemical imaging revealing the sequential migration of Ni, Co, and Mn upon the battery cycling of layered cathode. *Nano Lett.* 17, 3946–3951.
114. Suntivich, J., May, K.J., Gasteiger, H.A., Goodenough, J.B., and Horn, Y.S. (2011). A perovskite oxide optimized for oxygen evolution catalysis from molecular orbital principles. *Science* 3374, 1385–1386.
115. Zhou, S., Miao, X., Zhao, X., Ma, C., Qiu, Y., Hu, Z., Zhao, J., Shi, L., and Zeng, J. (2016). Engineering electrocatalytic activity in nanosized perovskite cobaltite through surface spin-state transition. *Nat. Commun.* 7, 11510.
116. Keast, V.J., Scott, A.J., Brydson, R., Williams, D.B., and Bruley, J. (2001). Electron energy-loss near-edge structure—a tool for the investigation of electronic structure on the nanometre scale. *J. Microsc.* 203, 135–175.
117. Haruta, M., Kurata, H., Komatsu, H., Shimakawa, Y., and Isoda, S. (2009). Site-resolved oxygen-K-edge ELNES of the layered double perovskite La₂CuSnO₆. *Phys. Rev. B* 80, 165123.
118. Ortiz-Medina, J., Kitano, H., Morelos-Gomez, A., Wang, Z., Araki, T., Kang, C.-S., Hayashi, T., Takeuchi, K., Kawaguchi, T., Tanioka, A., et al. (2016). Nanostructured carbon-based membranes: nitrogen doping effects on reverse osmosis performance. *NPG Asia Mater.* 8, e258.

119. Muller, D., Yujiun, T., Rishi, R., and John, S. (1993). Mapping sp^2 and sp^3 states of carbon at sub-nanometre spatial resolution. *Nature* 366, 725–727.
120. Hamon, A.-L., Verbeeck, J., Schryvers, D., Benedikt, J., and vd Sanden, R.M. (2004). ELNES study of carbon K-edge spectra of plasma deposited carbon films. *J. Mater. Chem.* 14, 2030–2035.
121. Su, Y.F., Park, J.G., Koo, A., Trayner, S., Hao, A., Downes, R., and Liang, R. (2016). Characterization at atomic resolution of carbon nanotube/resin interface in nanocomposites by mapping sp^2 -bonding states using electron energy-loss spectroscopy. *Microsc. Microanal.* 22, 666–672.
122. Schmid, H.K., and Mader, W. (2006). Oxidation states of Mn and Fe in various compound oxide systems. *Micron* 37, 426–432.
123. Nyquist, S., and Hälenius, U. (2013). An EELS study of near edge structures of the oxygen K-edge in spinels. *Phys. Chem. Miner.* 41, 255–265.
124. Chu, Y., Guo, L., Xi, B., Feng, Z., Wu, F., Lin, Y., Liu, J., Sun, D., Feng, J., Qian, Y., et al. (2018). Embedding $MnO@Mn_3O_4$ nanoparticles in an N-doped-carbon framework derived from Mn-organic clusters for efficient lithium storage. *Adv. Mater.* 30, e1704244.
125. Sun, R., Wang, Z., Shibata, N., and Ikuhara, Y. (2015). A dislocation core in titanium dioxide and its electronic structure. *RSC Adv.* 5, 18506–18510.
126. Chen, K.F., Lo, S.C., Chang, L., Egerton, R., Kai, J.J., Lin, J.J., and Chen, F.R. (2007). Valence state map of iron oxide thin film obtained from electron spectroscopy imaging series. *Micron* 38, 354–361.
127. Wang, Z.-L., Yin, J.-S., and Jiang, Y.-D. (2000). EELS analysis of cation valence states and oxygen vacancies in magnetic oxides. *Micron* 31, 571–580.
128. Daulton, T.L., and Little, B.J. (2006). Determination of chromium valence over the range Cr(0)-Cr(VI) by electron energy loss spectroscopy. *Ultramicroscopy* 106, 561–573.
129. James, H.P., and Ondrej, L.K. (1990). Elnes of 3d transition-metal oxides: II. Variations with oxidation state and crystal structure. *Ultramicroscopy* 32, 319–325.
130. Maras, E., Saito, M., Inoue, K., Jónsson, H., Ikuhara, Y., and McKenna, K.P. (2019). Determination of the structure and properties of an edge dislocation in rutile TiO_2 . *Acta Mater.* 163, 199–207.
131. Craven, A.J., Sawada, H., McFadzean, S., and McLaren, I. (2017). Getting the most out of a post-column EELS spectrometer on a TEM/STEM by optimising the optical coupling. *Ultramicroscopy* 180, 66–80.
132. Hou, C., Han, J.-H., Liu, P., Yang, C.-C., Huang, G., Fujita, T., Hirata, A., and Chen, M.-W. (2019). Operando observations of SEI film evolution by mass-sensitive scanning transmission electron microscopy. *Adv. Energy Mater.* 9, 1902675.
133. Zhang, W., Seo, D.H., Chen, T., Wu, L.-J., Topsakal, M., Zhu, Y.-M., Lu, D.-Y., Ceder, G., and Wang, F. (2020). Kinetic pathways of ionic transport in fast-charging lithium titanate. *Science* 367, 1030–1034.
134. Zhang, H., Meng, Y.-S., and Zhu, Y. (2015). Frontiers of in situ electron microscopy. *MRS Bull.* 40, 12–18.
135. Barwick, B., Park, H.S., Kwon, O., Baskin, J.S., and Zewail, A.H. (2008). 4D imaging of transient structures and morphologies in ultrafast electron microscopy. *Science* 322, 1227–1231.
136. Hwang, S., Chen, X., Zhou, G., and Su, D. (2019). In situ transmission electron microscopy on energy-related catalysis. *Adv. Energy Mater.* 10, 191902105.
137. Yang, J., Koo, J., Kim, S., Jeon, S., Choi, B.K., Kwon, S., Kim, J., Kim, B.H., Lee, W.C., Lee, W.B., et al. (2019). Amorphous-phase-mediated crystallization of Ni nanocrystals revealed by high-resolution liquid-phase electron microscopy. *J. Am. Chem. Soc.* 141, 763–768.
138. Moore, G.W.K., Howell, S.E.L., Brady, M., Xu, X., and McNeil, K. (2021). Anomalous collapses of Nares Strait ice arches leads to enhanced export of Arctic sea ice. *Nat. Commun.* 12, 1.
139. Lee, S.Y., Wu, L., Poyraz, A.S., Huang, J., Marschilok, A.C., Takeuchi, K.J., Takeuchi, E.S., Kim, M., and Zhu, Y. (2017). Lithiation mechanism of tunnel-structured MnO_2 electrode investigated by in situ transmission electron microscopy. *Adv. Mater.* 29, e1703186.
140. Shao, R., Chen, S., Dou, Z., Zhang, J., Ma, X., Zhu, R., Xu, J., Gao, P., and Yu, D. (2018). Atomic-scale probing of reversible Li migration in 1T- $V_{1+x}Se_2$ and the interactions between interstitial V and Li. *Nano Lett.* 18, 6094–6099.
141. Liu, F., Liu, S.-Y., Meng, J.-S., Xia, F.-J., Xiao, Z.-T., Liu, Z., Li, Q., Wu, J.-S., and Mai, L.-Q. (2020). Stabilizing conversion reaction electrodes by MOF derived N-doped carbon shell for highly reversible lithium storage. *Nano Energy* 73, 104758.
142. Liu, Y., Liu, Q., Jian, C., Cui, D., Chen, M., Li, Z., Li, T., Nilges, T., He, K., Jia, Z., et al. (2020). Red-phosphorus-impregnated carbon nanofibers for sodium-ion batteries and liquefaction of red phosphorus. *Nat. Commun.* 11, 2520.
143. Xiong, Y., Yang, Y., Joress, H., Padgett, E., Gupta, U., Yarlagadda, V., Agyeman-Budu, D.N., Huang, X., Moylan, T.E., Zeng, R., et al. (2019). Revealing the atomic ordering of binary intermetallics using in situ heating techniques at multilength scales. *Proc. Natl. Acad. Sci. U.S.A.* 116, 1974–1983.
144. Ophus, C. (2019). Four-dimensional scanning transmission electron microscopy (4D-STEM): from scanning nanodiffraction to ptychography and beyond. *Microsc. Microanal.* 25, 563–582.
145. Alamgir, F.M., Ito, Y., Jain, H., and Williams, D.B. (2014). Extended energy-loss fine structure analysis of 3d transition metals using ionization edges. *Philos. Mag. Lett.* 5, 4345.
146. James, L.H., Andrew, C.L., Li, Y.Y., Kanit, H., Anatoly, I.F., and Mitra, L.T. (2019). A synchrotron in the TEM: spatially resolved fine structure spectra at high energies. arXiv. <https://arxiv.org/abs/1909.06323>, arXiv:1909.06323v1.
147. Mizoguchi, T., and Kiyohara, S. (2020). Machine learning approaches for ELNES/XANES. *Microscopy (Oxf)* 69, 92–109.
148. Park, J., Lee, Y., Lee, H., and Ko, H. (2020). Transfer printing of electronic functions on arbitrary complex surfaces. *ACS Nano* 14, 12–20.